ECAP-2019-009

Sensitivity to tau-neutrino appearance with the first seven strings of KM3NeT/ORCA

Masterarbeit aus der Physik

vorgelegt von
Lukas Maderer
16. Mai 2019

Erlangen Centre for Astroparticle Physics
Physikalisches Institut IV
Friedrich-Alexander-Universität Erlangen-Nürnberg

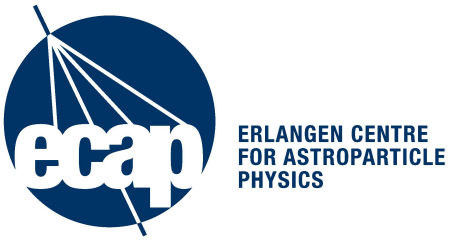

1. Gutachter: PD Dr. Thomas Eberl
2. Gutachter: Prof. Dr. Gisela Anton

Contents

1 Introduction

Neutrino physics plays a major role in modern science. From the postulation of the neutrino in 1930 by Pauli it took over 20 years for the first observation. To date there are still many open questions about neutrinos, like their absolute masses, if they violate CP-symmetry or if neutrino and anti-neutrino are the same particle (Majorana particle). Also it is not clear if the so far assumed three-neutrino-framework is complete, or if one or more additional neutrino flavour(s), e.g sterile neutrinos that mainly interact via gravitation, exist. All these questions come from the fact, that neutrinos are very difficult to detect, although they are produced in every nuclear reaction, our atmosphere, stars and most extragalactic objects. Because neutrinos can only interact via the weak force, have no electrical charge and very low masses, their interaction cross sections are in the order of $10^{-38}\,\mathrm{cm}^2 (at \sim 100\,\mathrm{GeV})$[1]!
To collect enough event statistic, physicist started to build huge detectors with large instrumented volumes, e.g. SuperKamiokande ($50 \cdot 10^3\,\mathrm{m}^3$)[2], Antares ($0.01\,\mathrm{km}^3$)[3] and IceCube ($1\,\mathrm{km}^3$)[4]. With this new generation of neutrino detectors, groundbreaking progress was made in the last decades, like the detection of galactic neutrinos (Nobel Prize 2002) and the detection of neutrino oscillations (Nobel Prize 2015).
Two future neutrino detectors are planned by the KM3NeT Collaboration: ARCA and ORCA (Astroparticle & Oscillation Research with Cosmics in the Abyss), water Cherenkov detectors that are going to be build in the Mediterranean sea. While ARCA will measure cosmic neutrinos, ORCA will be the worlds largest neutrino detector for low-energy atmospheric neutrinos, with an energy threshold of $\mathrm{E}_{\mathrm{thresh}} \sim 1\,\mathrm{GeV}$. Thus it will be capable of measuring the atmospheric neutrino flux, and be able to determine the so far unknown neutrino mass hierarchy, i.e. the order of the neutrino mass eigenstates, by the measured oscillation patterns. In addition, ORCA will also measure unprecedented numbers of tau-neutrino events. ν_τ-appearance studies with ORCA can therefore test oscillation parameters and the mandatory unitarity of the PMNS matrix in the three-neutrino-framework.
In this thesis the question is studied, whether it is possible to study ν_τ-appearance during the first building phase of the ORCA detector. In March 2019 one operating string was deployed, several others will follow during the rest of the year. For this work a data sample simulated for a possible future 7-string array is analysed. It shows that both the energy and zenith angle resolution, as well as event detection and selection efficiencies are sufficient to exclude a ν_τ-non-appearance at $3\,\sigma$ C.L. after about 6 months of measurement with the 7-string detector.

2 Scientific background

2.1 Neutrino physics

2.1.1 Status of neutrino physics

The neutrino was postulated for the first time by Pauli in 1930 [5]. He had two reasons for his theory, both coming from the β^--decay $n \to p + e^- + \bar{\nu}_e$. First, if one measures the energy of electrons produced in this decay, one receives a continuous energy spectrum. Because of energy conservation, the missing energy has to be carried away by a third, undetected particle, the neutrino. Second, due to conservation of angular momentum, and $J_p = J_n$ and $J_e = \frac{1}{2}$ a third particle with $J = \frac{1}{2}$ has to be produced.
Until the discovery of the neutrino 25 years passed. In 1956 Reines (Nobel Prize 1995) and Cowan measured the inverse β-decay $\bar{\nu}_e + p \to n + e^+$ and set the foundation for neutrino physics. At this point the following attributes of neutrinos are known:

- No electrical charge
- No magnetic moment
- Only interact via the weak force (and gravitation)
- Spin $S = \frac{1}{2}$

This leads to very small cross-sections for neutrino interactions (see subsection 2.1.4), the reason why it took so long to detect them.
Despite of huge improvements in the detection of neutrinos, there are still fundamental questions to be adressed. Thus many neutrino experiments are running or planned around the globe, e.g. KATRIN (determination of the neutrino mass) or GERDA (search for neutrino-less double beta-decay $0\nu\beta\beta$).

2.1.2 Neutrino oscillations

A milestone in neutrino physics was the discovery of neutrino oscillations, which was rewarded with a Nobel Prize in 2015, and describes how the flavour of a neutrino can change during its propagation through space. In the standard model of particle physics, for each charged lepton e, μ, τ a corresponding neutrino flavour ν_e, ν_μ, ν_τ exists. Measurements from the LEP collider at CERN confirmed this assumption from measurements of the Z-boson decay width [6], although it is not yet excluded that more neutrino types

exist beyond the standard model, e.g. sterile neutrinos that predominantly interact via gravitation. When the solar neutrino flux was measured by independent experiments (Homestake[7], Kamiokande[8], SAGE[9], GALLEX[10]) a deficit of ν_e compared to the "Standard Solar Model" (SSM) was detected. Since both the model and the experiment seemed to be correct, the theory of neutrino oscillations came to play. In this theory neutrino flavours are described as a mixture of so called mass eigenstates. The flavour eigenstates are important for neutrino interactions, e.g. flavour conservation, while the mass eigenstates describe the free propagation of neutrinos. The compositions of the three flavour eigenstates (e, μ, τ) via the mass eigenstates (1,2,3) are described by the unitary PMNS-matrix U:

$$\begin{aligned}\begin{pmatrix}\nu_e\\ \nu_\mu\\ \nu_\tau\end{pmatrix} &= \begin{pmatrix}U_{e1} & U_{e2} & U_{e3}\\ U_{\mu1} & U_{\mu2} & U_{\mu3}\\ U_{\tau1} & U_{\tau2} & U_{\tau3}\end{pmatrix} \times \begin{pmatrix}\nu_1\\ \nu_2\\ \nu_3\end{pmatrix}\\ &= \begin{pmatrix}c_{12}c_{23} & s_{12}c_{13} & s_{13}\\ -s_{12}c_{23} - c_{12}s_{23}s_{13} & c_{12}c_{23} - s_{12}s_{13} & s_{23}c_{13}\\ s_{12}s_{23} - c_{12}c_{23}s_{13} & -c_{12}s_{23} - s_{12}c_{23}s_{13} & c_{23}c_{13}\end{pmatrix} \times \begin{pmatrix}\nu_1\\ \nu_2\\ \nu_3\end{pmatrix}\end{aligned} \tag{2.1}$$

with $s_{ij} = \sin\Theta_{ij}$, $c_{ij} = \cos\Theta_{ij}$ and the mixing angles $\Theta_{12,23,13}$. Note that in the neutrino sector the CP-symmetry may not be conserved (which has not yet been observed), which would add a CP-violation phase δ_{CP} to the PMNS matrix. In this thesis δ_{CP} is assumed to be zero and is therefore not included in the following calculations[1]. The same holds for two potential Majorana-phases, that depends on whether the neutrino is a Dirac- or Majorana-particle, but has no influence on oscillations [11].

One can illustratively describe neutrino oscillations as follows: If $m_1 \neq m_2 \neq m_3$ holds true, all mass eigenstates travel with different velocities. After a certain propagation length L the phases of the mass eigenstates have shifted relative to each other compared to their original phase relation. If one would detect the neutrino, the composition of the mass eigenstates has changed and one would measure a different neutrino flavour with a certain probability.

A quantitative description of neutrino oscillations can be derived from Schroedinger's equation, starting with the relation from eq. 2.1

$$|\nu_\alpha\rangle = \sum_i U_{\alpha i}|\nu_i\rangle \ , \ |\nu_i\rangle = \sum_i (U^+)_{i\alpha}|\nu_\alpha\rangle \tag{2.2}$$

with $\alpha \,\epsilon\, [e, \mu, \tau]$ and $i \,\epsilon\, [1, 2, 3]$. Now from

$$i\frac{d}{dt}\begin{pmatrix}\nu_1(t)\\ \nu_2(t)\\ \nu_3(t)\end{pmatrix} = H_0 \begin{pmatrix}\nu_e(t)\\ \nu_\mu(t)\\ \nu_\tau(t)\end{pmatrix} \tag{2.3}$$

[1] Figure A.1 shows how the oscillation probabilities without CP-violation change for $\delta_{\mathrm{CP}} = 305°$. It does not affect the relevant energy range for ν_τ-appearance studies (see section 3.5)

with

$$H_0 = \begin{pmatrix} E_1 & 0 & 0 \\ 0 & E_2 & 0 \\ 0 & 0 & E_3 \end{pmatrix} \tag{2.4}$$

the time evolution of a neutrino flavour can be written as

$$|\nu_\alpha\rangle = \sum_i U_{\alpha i} e^{-iE_i t} |\nu_i\rangle \ . \tag{2.5}$$

The probability of a neutrino to oscillate from flavour eigenstate $\nu_\alpha \to \nu_\beta$ is then the square of the transition amplitude:

$$P(\alpha \to \beta; t) = |\psi_{\alpha\beta}|^2 = |\langle \nu_\beta | \nu_\alpha(t)|^2 \ . \tag{2.6}$$

With the relativistic approximation

$$E_i = \sqrt{p^2 + m_i^2} \approx p + \frac{m_i^2}{2p} \approx E + \frac{m_i^2}{2E} \tag{2.7}$$

one gets

$$P(\alpha \to \beta; t) = \delta_{\alpha\beta} - 4 \sum_{j>i} U_{\alpha i} U_{\alpha j} U_{\beta i} U_{\beta j} \sin^2 \frac{\Delta_{ij}}{2} \tag{2.8}$$

where

$$\Delta_{ij} = \frac{E_i - E_j}{\hbar} t = 2.534 \frac{\Delta m_{ij}^2}{\mathrm{eV}^2} \cdot \frac{L/\mathrm{km}}{E/\mathrm{GeV}} \ . \tag{2.9}$$

The important values for neutrino oscillations are therefore:

- Mass differences of the mass eigenstates $\Delta m^2_{12}, \Delta m^2_{23}$
- Mixing angles $\Theta_{12}, \Theta_{13}, \Theta_{23}$
- Neutrino energy E
- Propagation length L

From the observed oscillations one can therefore conclude that $\Delta m^2_{12}, \Delta m^2_{23} \neq 0$ and consequently that neutrinos have mass in contrast to the SM, where neutrinos are assumed to be massless. Thus, studies of neutrino oscillations could reveal physics beyond the standard model and are investigated by many experiments, like KamLAND, Super-Kamiokande and Homesteak (reactor, atmospheric and solar neutrinos, respectively). Another conclusion from Equation 2.8 is that one can decide which oscillation channel one wants to measure with an experiment, by choosing the correct neutrino source (hence E) and distance L between detector and source. For $\Delta m^2_{23} \sim 10^{-3}\,\text{eV}$ and atmospheric length scales $L \sim 10^4\,\text{km}$ one expects neutrino oscillations for $E_\nu \sim 10\,\text{GeV}$, which is consequently the energy range that ORCA is designed for.

2.1.3 Mass ordering and MSW-effect

One big question of neutrino physics is the so called mass hierarchy, i.e. the ordering of the mass eigenstates (fig. 2.1). It is not trivial to answer this question, because the oscillation probability only depends on the absolute value of Δm^2_{ij} . Although the mass hierarchy is not important for the studies of this thesis, it will be briefly discussed here, since it is the main purpose of ORCA to determine the sign of Δm^2_{23}.

If neutrinos propagate through matter, due to the presence of electrons and possible charged current ν_e-e reactions (e.g. coherent elastic scattering) oscillation probabilities change with respect to oscillations in vacuum [13]. The new oscillation probabilities, can be calculated by adding a phase shift proportional to the refraction index of the traversed matter to the Hamilton matrix in Equation 2.3. This leads after some math (see [5] chapter 6.6) to a new mixing matrix $U(\Theta) \rightarrow U_m(\Theta_m)$ in matter and especially to new oscillation probabilities:

$$P_m(\nu_\alpha \rightarrow \nu_\beta) \sim \sin^2\Theta_m = \frac{\sin 2\Theta}{\sqrt{(\frac{A}{D} - \cos 2\Theta)^2 + \sin^2 2\Theta}} \tag{2.10}$$

where

$$A = 2\sqrt{2} G_F N_e p \; ; \; D = m_j^2 - m_i^2 \; . \tag{2.11}$$

Here G_F is the Fermi coupling constant, N_e the electron density and p the neutrino momentum. From Equation 2.10 one sees that for $\frac{A}{D} = \cos(2\Theta)$ the oscillation probability

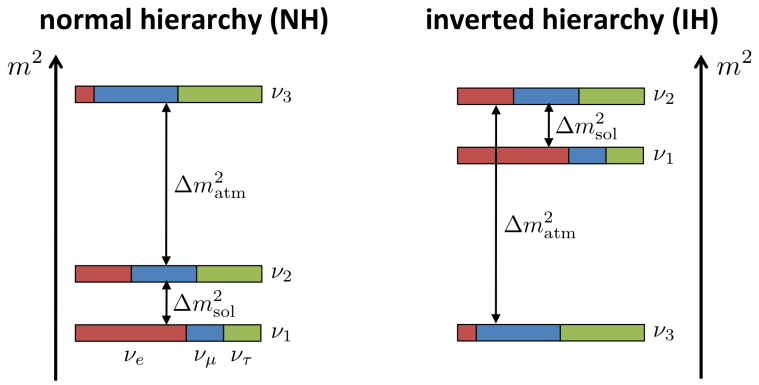

Figure 2.1: The two possible neutrino mass orderings [12]. On the left side $\nu_3 > \nu_{1/2}$ (normal hierarchy), on the right side $\nu_3 < \nu_{1/2}$ (inverted hierarchy). The colors illustrate the composition of the mass eigenstates by the flavour eigenstates.

reaches a maximum - even for small mixing angles Θ and mass differences D. This resonance in the oscillation probability is called MSW-effect and was confirmed by solar neutrino experiments [7][8][9][10].
The key factor for the link between the MSW-effect and the determination of the neutrino mass hierarchy is the sign of A. Due to $A \rightarrow -A$ for $\bar{\nu}$ the MSW-effect only occurs for neutrinos or anti-neutrinos, depending on the sign of D. Since only ν_e are produced in the sun [5] one could conclude from the observed MSW-effect that $m_2 > m_1$. For the $\Delta m^2_{23} = 2.44 \cdot 10^{-3}\,\text{eV}^2$ one needs to go to higher neutrino energies to reach oscillation resonances. ORCA is therefore designed for the measurement of atmospheric neutrinos. For the density profile of the earth (fig. 2.2) and a baseline L up to $\sim 12\,000\,\text{km} = 2 \cdot r_{\text{Earth}}$ (depending on the zenith angle of the incoming neutrino) one expects matter resonances for neutrinos with $E = 3\text{-}10\,\text{GeV}$.

2.1.4 Tau-neutrino cross section

The understanding of neutrino cross sections is an essential part of every neutrino experiment. Yet, the theoretical prediction of neutrino cross sections are complex, because many factors have to be considered, that can be completely different for different energy regimes. For the energy range relevant for ORCA ($E\,\epsilon\,[1, 100]\,\text{GeV}$), three neutrino-matter interaction mechanisms play a role [15]:

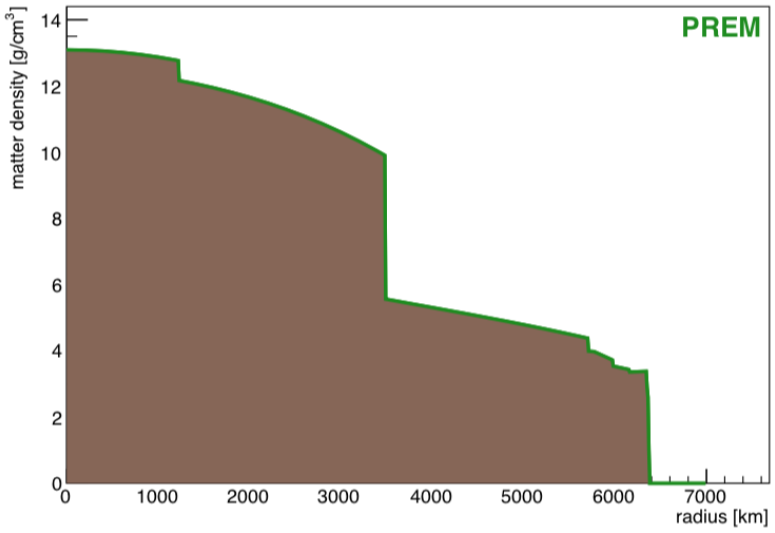

Figure 2.2: Preliminary reference Earth model (PREM) [14]

- **(quasi-)elastic scattering**: the neutrino scatters with the whole nucleus, liberating one ore more nucleons. In case of charged current (neutral current), one speaks of (quasi-)elastic scattering.
- **resonance production**: the nucleon gets excited into a resonance state and decays in other nucleons and/or mesons.
- **deep inelastic scattering (DIS)**: the neutrino scatters with partons inside the nucleus, causing a hadronic shower.

Each interaction mechanism is dominant at different energies. Figure 2.3 gives an overview about the total (anti-)neutrino (ν_μ) charged current cross section over the energy and the respective contributions of each scattering mechanism.
The cross section of ν_τ is strongly influenced by the high mass of the τ lepton. This leads to a strong suppression of the cross section $\sigma(\nu_\tau)$ for energies below the so called tau turn-on at 3.5 GeV.
The first experimental determination of the tau-neutrino cross section came from the DONuT experiment [16]. They looked at neutrinos that were produced in collisions of 800 GeV-protons from the Fermilab Tevatron with a beam dump. About 3% of the neutrinos were ν_τ (no $\bar{\nu}_\tau$) and were produced in decays of charmed particles (prompt neutrinos). From nine observed ν_τCC events[2] with $E_\nu > 100\,\text{GeV}$, DONuT received an estimated value for the energy-independent cross section (deep inelastic scattering dominates) of $\sigma_{\text{const}}(\nu_\tau) = (0.39 \pm 0.13 \pm 0.13) \cdot 10^{-38}\,\text{cm}^2\text{GeV}^{-1}$, with statistical and systematic error.
A second measurement of the tau-neutrino cross section was delivered by SuperKamiokande

[2]Note that the analysis used in [16] could not distinguish between ν_τ and $\bar{\nu}_\tau$.

[17]. From ν_τ-appearance measurements (similar to those discussed in this thesis) they measured an averaged tau-neutrino cross section for energies between 3.5 GeV and 70 GeV of $(0.94 \pm 0.20) \cdot 10^{-38}\,\mathrm{cm}^2$.
To compare their results, they extrapolated DONuT's result to lower energies with

$$\sigma(E) = \sigma_{\mathrm{const}} \cdot E \cdot K(E) \tag{2.12}$$

where $K(E)$ is the kinematic effect of the tau lepton mass. Furthermore, because SuperKamiokande detected many ν_τ below 10 GeV where DIS is suppressed, they had to scale their own result to 41%, which is the estimated ratio of DIS events in the SuperKamiokande data. This leads to an averaged tau-neutrino cross section between 3.5 GeV and 70 GeV of $(0.37 \pm 0.18) \cdot 10^{-38}\,\mathrm{cm}^2$ (DONuT) and $(0.40 \pm 0.08) \cdot 10^{-38}\,\mathrm{cm}^2$ (SuperKamiokande). These results are consistent with each other.
The theoretical uncertainties of the tau-neutrino cross section is in the order of $\mathcal{O}(10\%)$ [18]. In addition, the theory predicts $\sigma(\nu_\tau) > \sigma(\bar{\nu}_\tau)$ [17][18].

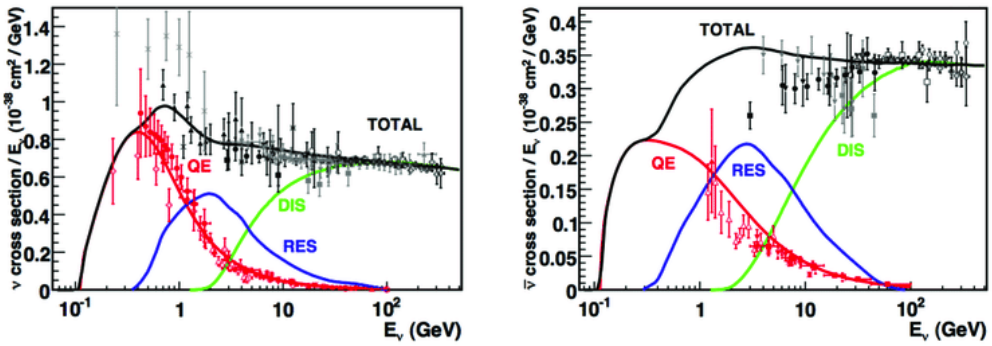

Figure 2.3: Total ν_μ and $\bar{\nu}_\mu$ per nucleon CC cross sections (for an isoscalar target) divided by neutrino energy. [15]

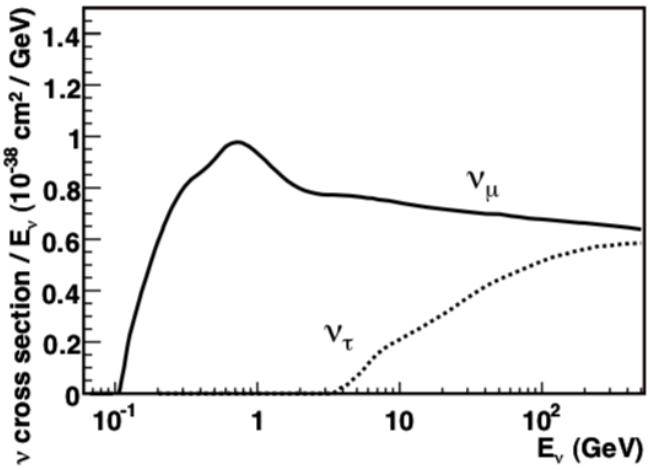

Figure 2.4: Comparison of $\sigma(\nu_\mu)$ and $\sigma(\nu_\tau)$ over the neutrino energy. The tau cross section is suppressed below the tau turn-on at 3.5 GeV [15].

2.1.5 Atmospheric neutrinos

Atmospheric neutrinos are produced by high-energetic cosmic rays that hit the Earth's atmosphere. The products of these interactions are mostly hadrons that again decay and produce a particle shower in the atmosphere. In most of these decays neutrinos are produced, too, mainly by the decay of pions and kaons:

$$\begin{aligned} \pi^- &\to \mu^- \bar{\nu}_\mu \to e^- \bar{\nu}_e \nu_\mu \bar{\nu}_\mu \\ K^- &\to \pi^- \pi^0 \\ &\to \mu^- \bar{\nu}_\mu \to e^- \bar{\nu}_e \nu_\mu \bar{\nu}_\mu \end{aligned} \tag{2.13}$$

provided that the muons decay before reaching the ground. Analogue decays take place for π^+ and K^+. Tau neutrinos are almost only produced in decays from mesons containing a charm quark, so called 'prompt neutrinos'. This production is strongly surpressed and therefore negligible [19]. Figure 2.5 shows different flux models for atmospheric neutrinos and the $\frac{(\nu_\mu+\bar{\nu}_\mu)}{(\nu_e+\bar{\nu}_e)}$-ratio over zenith and energy. The atmospheric neutrino flux follows a power-law spectrum

$$\phi_\nu(E) \sim E^{-\gamma} \tag{2.14}$$

with the spectral index $\gamma \approx 3$ [20]. Due to magnetic fields inside our Galaxy cosmic rays and therefore the atmospheric neutrino flux is approximately isotopic [21].
All figures in this thesis that contain information about flux rates in ORCA are based on the calculations of Honda et al.[22].

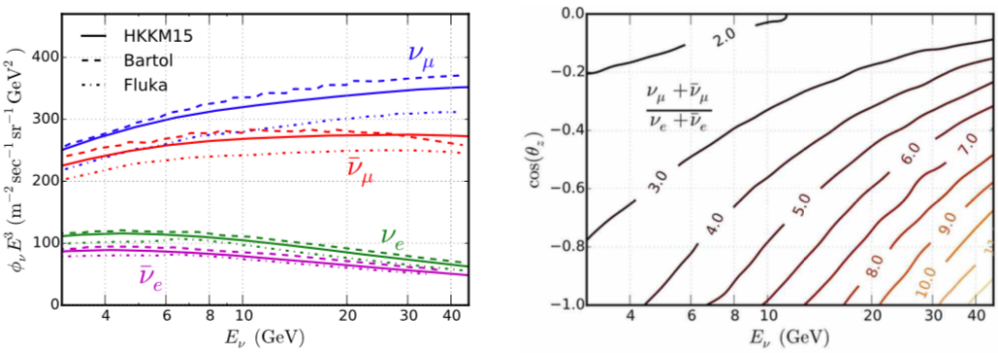

Figure 2.5: Left: Different flux models for the atmospheric neutrino flux $< 50\,\text{GeV}$, separated for electron/muon (anti-)neutrinos. Right: $\frac{(\nu_\mu+\bar{\nu}_\mu)}{(\nu_e+\bar{\nu}_e)}$-ratio over zenith and energy [23].

2.2 Learning from ν_τ-appearance

With ORCA one can carry out interesting physic studies, like constraining atmospheric oscillation parameters, or the measurement of the atmospheric muon flux. This thesis covers the so called ν_τ-appearance, the phenomenon of ν_τ[3] appearing in a detector with sources that are originally free from this neutrino flavour, like the atmospheric neutrino flux. This is possible due to neutrino oscillations. Although neutrino oscillations are measured and confirmed for many years now, the ν_τ sector is still relatively poorly explored, motivating sensitivity studies for tau-neutrinos with the ORCA detector. This section will provide a short overview over previous ν_τ-experiments and conclusions that can be derived from ν_τ-appearance.

2.2.1 Previous ν_τ-appearance experiments

The detection of ν_τ turned out to be experimentally complicated, mainly due to the lack of ν_τ-sources. So far no ν_τ-beam could be produced artificially and in the sun no ν_τ are produced. Thus the first evidence for ν_τ-appearance came from two neutrino oscillation experiments, SuperKamiokande and OPERA. A present publication to this topic comes from IceCube/DeepCore.
The SuperKamiokande detector is a huge water tank (50kt water) with PMTs at the inner mantle that detect Cherenkov light produced by secondary charged particles from neutrino-hadron interactions. The number of detected ν_τCC-events is estimated with their expected signature on a statistical basis, similar to the procedure used for ORCA. With this technique, evidence for ν_τ-appearance was found in 2018 with a data sample including $\sim 338\,\nu_\tau$-events [17].
Another approach to detect tau-neutrinos was made by the OPERA Collaboration, that investigated the pure LNGS ν_μ beam, pointing from CERN to the Gran Sasso Laboratory in Italy. Due to its high spatial resolution, tau-neutinos can be distinguished by their unique signature, i.e. two shower vertices close to each other. The first direct observation of a tau-neutrino canditate was reported in 2010 [24] with a significance of 2.01σ. 2018 ν_τ-appearance was confirmed with 6.1σ [25].
The latest publication comes from the IceCube Collaboration. With their DeepCore-detector, which has an energy-threshold slightly above the one from ORCA, the data of 3 years livetime exclude ν_τ-non-appearance with 3.2σ (2.0σ with only CC-interaction) [26]. Since the detection technique of IceCube DeepCore and KM3NeT/ORCA are similar, this is a reasonable reference value for the results of this thesis.

[3] Unless stated otherwise, ν_τ stands for both ν_τ and $\bar{\nu}_\tau$.

2.2.2 Physical motivation

Analogous to the quark-mixing, unitarity is expected in the 3-neutrino framework:

$$U^H U \stackrel{!}{=} \mathbb{1} \Rightarrow U^H = U^{-1} \, . \tag{2.15}$$

For the entries of the matrix one obtains 12 conditions that have to be fulfilled for unitarity (see [27]). Thus from measurements of the PMNS entries on can confirm its unitarity. So far the constraints on the unitarity are poor [28], which is mainly due to the high uncertainties in the tau-sector (up to 104% in the case of $|U_{\tau 3}|$).

ν_τ-appearance measurements are suited for the testing of the unitarity in the ν_3 mass eigenstate:

$$|U_{e3}|^2 + |U_{\mu 3}|^2 + |U_{\tau 3}|^2 \stackrel{!}{=} 1 \, . \tag{2.16}$$

Global fits show that $|U_{e3}|^2 + |U_{\mu 3}|^2 \simeq 0.5$ leading to an expectation of $|U_{\tau 3}| \simeq 0.5$. The current 3σ range is at $|U_{\tau 3}|^2 = 0.16 \rightarrow 0.61$ [28], limiting Equation 2.16 to $0.56 \rightarrow 1.24$. The IceCube DeepCore experiment achieves the 90% confidence interval on the tau-sector unitarity of $0.34 \rightarrow 1.30$ [26]. Further measurements are mandatory in order to get reliable statements on the unitarity of the PMNS.

3 ν_τ-appearance in ORCA

3.1 Detection technique

The detection of neutrinos is experimentally challenging. First evidence for neutrinos came from chemical experiments. Here, the detector contains a specific element, that changes due to neutrino-nucleon interactions. The number of resulting isotopes is counted and the neutrino flux passing the detector can be estimated. However, energy, time and direction information of the neutrinos get lost with this technique.
To get the idea behind the water Cherenkov technique used in KM3NeT, one has to look at neutrino-nucleon interactions (fig. 3.1). Since neutrinos can only interact via the weak force, they exchange either a $W^\pm$ (charged current, CC) or a Z^0 (neutral current; NC) with the nucleon. In both cases this leads to a destruction of the nucleon and a hadronic particle shower at the interaction point (vertex).
The charged particles in the shower are accelerated to velocities above the speed of light in water, since $E_\nu \gg m_{\text{hadron}}$, and produce Cherenkov light [29], which is radiated conical in the direction of the charged particle at the Cherenkov angle

$$\Theta_{\text{Cher}} = \cos^{-1}(\frac{1}{\beta n})\,. \tag{3.1}$$

With the refraction index in seawater $n_{\text{sea}} \approx 1.35$ and for relativistic particles $\beta \approx 1$ one receives $\Theta^{\text{sea}}_{\text{Cher}} \approx 42°$.
Depending on the exchanged boson, the neutrino converts into a charged lepton (CC) or not (NC). The charged lepton produced in νCC interactions produces again Cherenkov light. From the light pattern one can draw a conclusion on the lepton family (e, μ, τ). While an electron produces an electromagnetic shower immediately (**shower-like** event), a muon travels $\sim 4\,\text{m}$ per GeV before it has lost its entire energy and drops below the Cherenkov threshold, leaving a **track-like** light signature inside the detector.
Other than in Figure 3.1 at the atmospheric energy scale (GeV) the τ decays after few mm, due to its short lifetime ($\sim 10^{-13}\,\text{s}$), which is not resolvable in ORCA. Therefore ν_τCC interaction signatures depend on the decay channel of the τ. Possible decay channels with branching ratios are listed in Table 3.1. Only one channel produces a μ with a BR of 17%. Therefore most of the ν_τCC have a shower-like signature.
NC interactions between neutrino and nucleon produce only a hadronic shower , since the neutrino leaves the detector without further interactions. On the one hand, this makes it impossible to gain information about the neutrino flavour through the detector

Decay mode	Branching ratio (%)
$e^-\bar{\nu}_e\nu_\tau$	17.83
$\mu^-\bar{\nu}_\mu\nu_\tau$	17.41
$\pi^-\nu_\tau$	10.83
$\pi^-\pi^0\nu_\tau$	25.52
$3\pi\nu_\tau$	18.29
others	10.12

Table 3.1: Decay channels for the τ [17]. Except the second decay mode, with a branching ratio of 17.41 %, all decay products lead to an shower-like signature in the detector.

signature of a lepton. On the other hand, the neutrino energy can not be estimated, since it transfers only a fraction of its energy to the nucleon[5].
For the whole analysis in this thesis, only CC-events were considered.

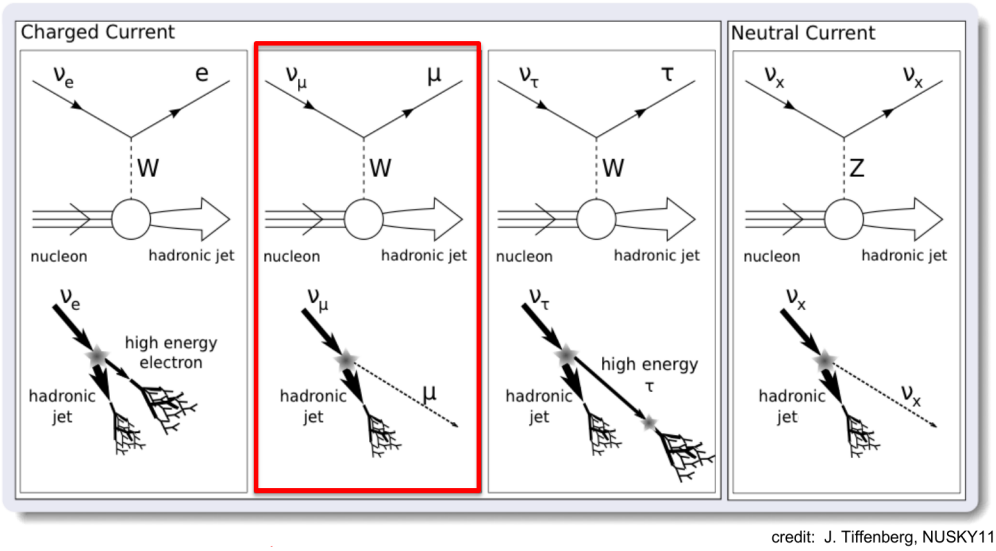

Figure 3.1: Possible neutrino interactions for all flavours, charged current (CC) and neutral current (NC) with Feynman diagrams and resulting signatures [30]. The pictured ν_τCC event where vertex and the shower resulting from the τ-decay are separated significantly only holds true for high E_ν.

3.2 KM3NeT/ORCA setup

The ORCA detector will be deployed in the Mediterranean sea, 40km offshore from Toulon in a depth of 2450km [23]. It consists of 115 detection units (DU) – "strings" – with

Figure 3.2: Left: Detection string; Right: single DOM [23]

18 digital optical modules (DOM) that hosts 31 photomultiplier tubes for the detection of Cherenkov light. The strings are spaced about 20m (horizontal) to each other. The DOMs of each string have a spacing of 9m. The complete infrastructure at the detection site is shown in Figure 3.3 with an instrumented volume of about $\sim 8 \cdot 10^6\,\mathrm{m}^3$. Note that the horizontal spacing as well as the final string positions are not final yet. The digitised data of all PMTs is send on-shore for real time processing. Several trigger conditions are applied to extract events from the complete data that then get written on disk. Main criteria for the trigger come from causalities of time-positions correlations of PMT hits, i.e. signals that exceed a defined threshold. For the Monte Carlo simulation events are simulated inside a volume V_{sim} that is multiple times bigger than the instrumented volume. With

$$\frac{N_{\mathrm{triggered}}}{N_{\mathrm{simulated}}} \cdot V_{\mathrm{sim}} = V_{\mathrm{eff}} \tag{3.2}$$

one gets a measure for the effective volume V_{eff} that is often referred to. Multiplied with the density of sea water it gives the effective detector mass M_{eff} in Figure 3.4.

3.3 Background events

The two main sources of background in the ORCA detector are random noise events ($\sim 41\,\mathrm{Hz}$ trigger rate) and atmospheric muons events ($\sim 18\,\mathrm{Hz}$ trigger rate)[23]. Both rates are several orders magnitudes over the estimated rate of neutrino events ($\mathcal{O}(3.5\,\mathrm{mHz})$)

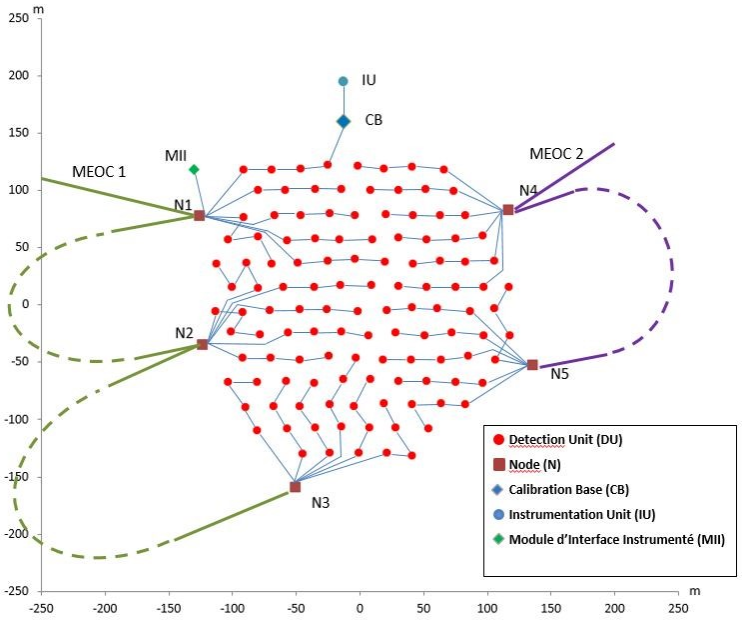

Figure 3.3: Preliminary ORCA layout with string positions and sea floor infrastructure [43].

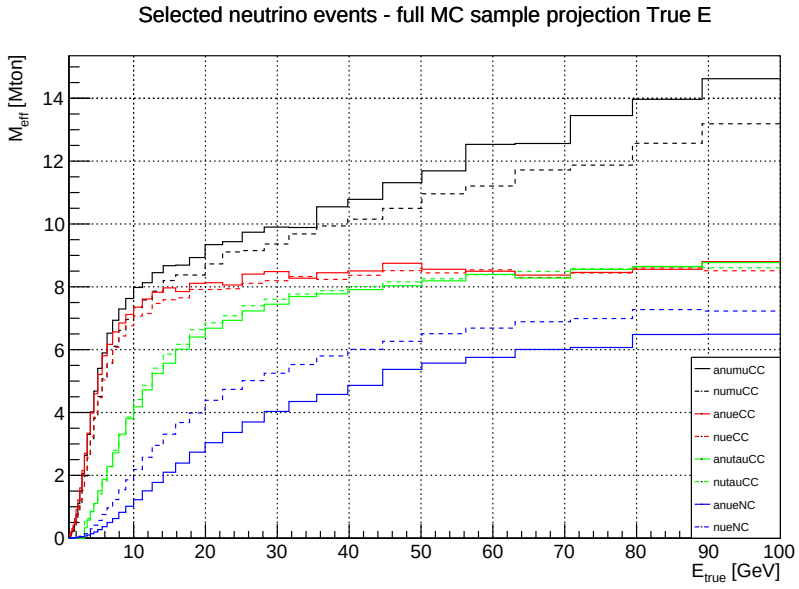

Figure 3.4: Effective detector mass for $\nu/\bar{\nu}$ CC+NC.The effective volume was calculated with selected events only (**??**. ((a)nueNC stands for all NC events)

and must therefore be separated from the neutrino events with a high efficiency. For the full detector this works fine with the combination of selection cuts, trigger conditions and machine learning.

Random noise events: The strongest source of optical background in the Mediterranean sea comes from radioactive decays of the potassium isotope K^{40}, whose decay products produce Cherenkov light. Noise events can be also triggered by random coincident signals in PMTs (dark noise) or by bioluminiscence in the deep sea [23].

Atmospheric muons: Atmospheric muons are produced in pion and kaon decays that have their origin in hadronic air showers produced by high energetic cosmic particles. Since one can not distinguish between atmospheric muons and muons from ν_μCC by their track-like signature, atmospheric muons have to be recognized based on the signal they generate in the detector. The three main criteria used to identify atmospheric muons are

1. **Direction:** Muons can not pass through the Earth $\rightarrow$ cut on up-going events ($\cos(\Theta_{\text{zenith}}) < 0$).
2. **Energy:** Most atmospheric muons that reach the detector have high energies $> 100\,\text{GeV}$.
3. **Vertex position:** Atmospheric muons that pass the energy criteria are usually reconstructed poorly, i.e. $E_{\text{reco}} << E_{\text{true}}$. This behaviour is expected to appear for atmospheric muons that pass the detector in a large distance, consequently deposit only a small fraction of light in the detector. Events with reconstructed vertex positions far away from the instrumented volume are therefore assumed to be atmospheric muons.

3.4 Data processing

After the data is send on-shore for the analysis it runs through the three following steps:

Event Reconstruction: All triggered events are processed by two reconstruction algorithms: Dusj and JGandalf, for shower- and track-like events, respectively [31][32]. Both reconstructions are designed to estimate from the PMT signals quantities like energy, direction and interaction position of the triggered event. From the number of registered hits the event energy can be estimated, while the time stamp of the signals in the detector gives information about the direction of the incoming particle.

Event selection: Not all events that were triggered and reconstructed are taken into account for further analysis. Some selection cuts on the reconstruction parameters were made by hand, to preselect events that might not be reconstructed with sufficient quality. They main criteria for an event to be selected are:

- The reconstructed vertex position has to be located inside or near the instrumented volume.
- The main part of the produced Cherenkov light has to be produced inside the instrumented volume. This can be estimated from the reconstructed vertex and direction of the event.
- The reconstruction must have a high confidence level. Both Dusj and JGandalf return a measure for the likelihood of the reconstructed values to be true.

The selection cuts are discussed in detail in chapter 4.

Particle identification (PID): For further analysis it is crucial to divide events into shower- and track-like. After the event reconstruction with Dusj and JGandalf, a random decision forest (RDF [45]) calculates the probability for each event to be a track or a shower (algorithm from [44]). Additionally, the RDF returns a score for each event to be an atmospheric muon (muon-score) or a random noise event (noise-score). It showed that a thoughtful pre-selection of events can improve the efficiency of the PID significantly.

3.5 ν_τ in ORCA

The ORCA detector is sensitive to the atmospheric neutrino flux, that consists (almost) only of ν_e and ν_μ. Nevertheless one expects to detect tau neutrinos at the ORCA site, due to neutrino oscillations. The main contribution comes from the $\nu_\mu \to \nu_\tau$ channel. For neutrinos, the oscillation probability is given by [26]:

$$P(\nu_\mu \to \nu_\tau) \simeq \cos^4(\Theta_{13}) \sin^2(2\Theta_{23}) \sin^2(\frac{\Delta m_{32} L}{4E}) \tag{3.3}$$

The baseline L is dependent on the angle of the incoming neutrino, varying from $\sim 20\,\text{km}$ (straight down-going; $\cos(\Theta_{\text{zenith}}) = 1$) to $\sim 12\,000\,\text{km}$ (straight up-going; $\cos(\Theta_{\text{zenith}}) = -1$). For all results presented in this thesis, only up-going events are considered, to suppress atmospheric muons (see section 3.3). The result of Equation 3.3 is shown in Figure 3.5 for the neutrino and anti-neutrino channel. Note: The pattern around 6 GeV and $\cos(\Theta_{\text{zenith}})$ in (a) comes from the MSW-effect, in case of normal mass ordering. With ORCA one tries to resolve this pattern and determine the true mass hierarchy.
Combining the atmospheric neutrino model (Honda [22], oscillation probabilities (global fit values [1]) and neutrino cross sections (Formaggio [15]) one can simulate how many events get triggered in the ORCA detector. The energy-zenith distribution of the expected detected event rates of tau-neutrinos in ORCA are plotted in Figure 3.6 (other flavours in Figure A.7). The main region where tau-neutrinos are expected is in the range $20\,\text{GeV} \lesssim E \lesssim 30\,\text{GeV}$ and $\cos(\Theta_{\text{zenith}}) \lesssim -0.4$. The zenith dependence of the expected

event rates comes from different propagation lengths and consequently different oscillation probabilities. Note that one expects $\sim 2-3$ times more ν_τ than $\bar{\nu}_\tau$ due to the higher cross section. The effect of the tau turn-on (no τ-production below 3.5 GeV) is clearly visible.
The amount of detected tau-neutrinos in ORCA is from now on referred to as ν_τ-normalisation (TauNorm):

$$\text{TauNorm} = \nu_{\text{Flux}} \cdot \text{oscillation probability} \cdot \text{cross section}\,. \tag{3.4}$$

The assumptions for neutrino flux, oscillation probability and cross section that were made in chapter 2 lead to a TauNorm equal 1, and an expectation of detected events as in Figure 3.6. Deviations from TauNorm=1 can consequently origin from each of the factors in Equation 3.4.
The following chapter describes the analysis and results of ORCA's sensitivity to ν_τ-appearance, for both the full detector and a multi-string detector that could be realised in 2019.

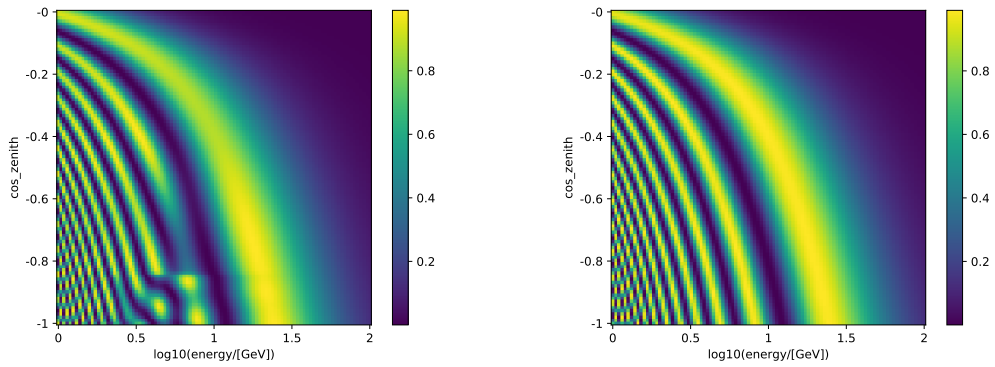

(a) (b)

Figure 3.5: Oscillation probabilities over $\cos(\Theta_{\text{zenith}})$ and log10(Energy/[GeV]) for **(a)** $\nu_\mu \to \nu_\tau$ and **(b)** $\bar{\nu}_\mu \to \bar{\nu}_\tau$ (normal hierarchy assumed).

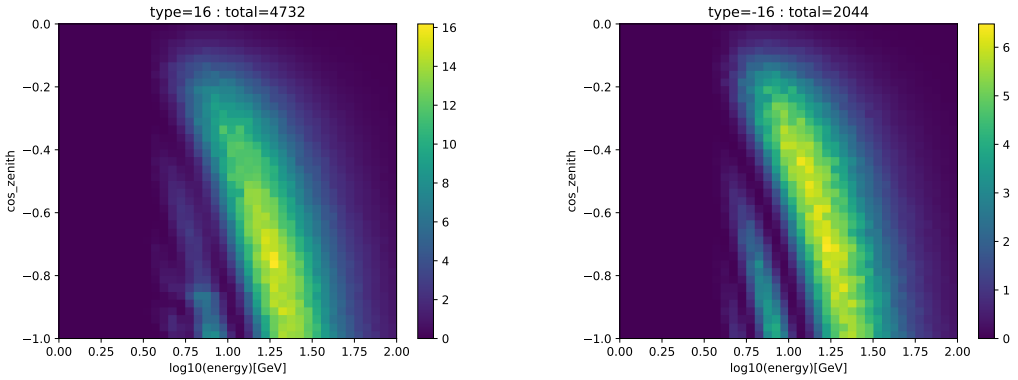

(a) ν_τ (b) $\bar{\nu}_\tau$

Figure 3.6: Expected tau-neutrino event rates in ORCA 115DU for one year.

4 Sensitivity studies to ν_τ-appearance

ORCA's sensitivity to ν_τ-appearance has been evaluated before by the KM3NeT group at ECAP [33]. At the time the study was published, no Monte Carlo simulation for a partial setup of ORCA has been produced. Nevertheless the analysis for the complete detector is a useful guideline for the analysis of a phase-1 detector. The software used in [33] is ParaNMH, designed by members of the KM3NeT collaboration. All results of this thesis were produced with the software package SWIM, for the reason that the detector response is entirely based on Monte Carlo simulations [34], which means that the analysis used for the 115 DU production can be applied to any other Monte Carlo data by simply changing the input file of the software. The first part of this thesis was therefore to reproduce the results of [33] to check for potential differences arising from the different frameworks used.

4.1 Sensitivity with SWIM

The ProfileTauNorm application implemented in SWIM is used for the calculation of ORCA's sensitivity to ν_τ-appearance. For every possible TauNorm a χ^2 value is returned as a measure of the likelihood with which the tested TauNorm can be excluded by the given data. The χ^2 calculation for one TauNorm N_{test} goes through the following steps:

1. Fill 2D-histogram "data" (cos-zenith vs. energy) with reconstruction output of simulated events (fig. 4.1 (a)).

2. Fill 2D-histogram "model" (cos-zenith vs. energy) based on a flux model, oscillation parameters and detector response matrix (fig. 4.1 (b)).

3. Fit "model" to "data" with **fixed TauNorm** $N_{\text{test}} \rightarrow$ calculate χ^2_{fixed} (Equation 4.1) (result in fig. 4.1 (c)).

4. Repeat fit with **free TauNorm** $\rightarrow$ calculate χ^2_{free}.

5. Return $\chi^2_{\text{fixed}} - \chi^2_{\text{free}} = \Delta\chi^2$

The χ^2 in step 3 & 4 is calculated as follows:

$$\begin{aligned}\chi^2(\text{model}, \text{data}) &= -2 \cdot \sum_{i=0}^{i=N_{Bins}} \ln P(\text{data}_i|\text{model}_i) - \ln P(\text{data}_i|\text{data}_i) \\ &= 2 \cdot \sum_{i=0}^{i=N_{Bins}} \text{model}_i - \text{data}_i + \text{data}_i \cdot \ln\left(\frac{\text{data}_i}{\text{model}_i}\right)\end{aligned} \tag{4.1}$$

using the 2D-histograms "data" and "model" after the fit converged. Step 3 & 4 are done twice, once with the starting value of Θ_{23} in the first octant ($< 45°$), once in the second octant ($> 45°$). The best fit of the free and fixed TauNorm fit is kept and used for step 5. All steps are done for each defined PID class, i.e. track and shower. In step 3 (calculation of χ^2) only up-going events with $\cos(\Theta_{\text{zenith}}) < 0$ are taken into account to reduce the amount of atmospheric muon events. Since the propagation length L of down-going events is rather short, only few oscillations into the tau-flavour and hence a low χ^2-contribution are expected. The final $\Delta\chi^2$ is the sum of the result of both the track and the shower class.
This calculation gives the confidence level $\sigma = \sqrt{\Delta\chi^2}$, with that the "model" with true TauNorm N_{test} can be excluded, under the assumption that "data" was measured by the detector.
In the example shown in Figure 4.1 a simulated data set with TauNorm = 1 (a) is tested for ν_τ-non-appearance (TauNorm = 0)(b). The resulting histogram (c) shows the χ^2 resulting from (a) and (b) and hence ORCA's sensitivity on ν_τ-appearance.

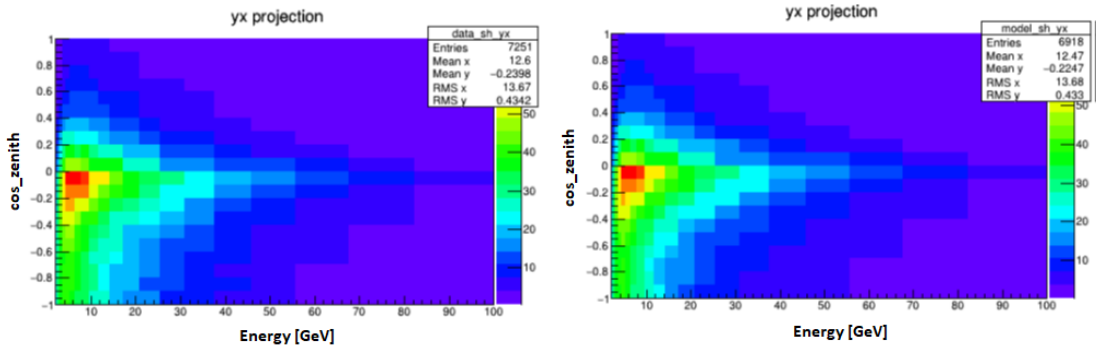

(a) Data

(b) Model

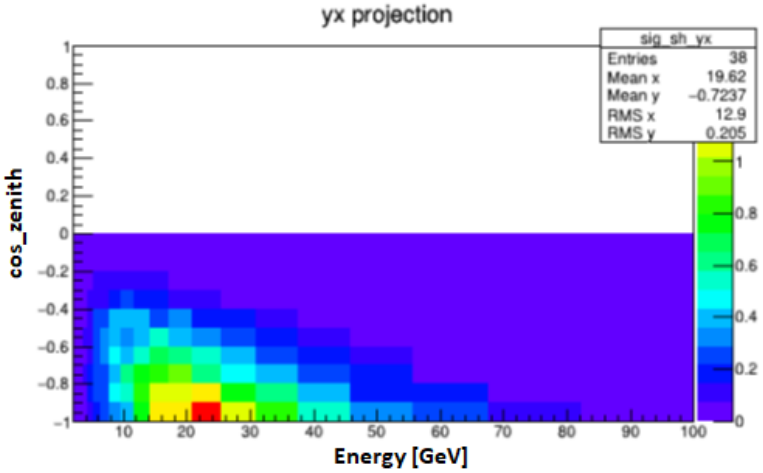

(c) χ^2 after Equation 4.1.

Figure 4.1: Visualisation of the sensitivity calculation. The model (b) is filled based on the Honda flux model, oscillation probabilities, neutrino cross sections and a detector response matrix and afterwards fitted to the data (a). The χ^2 is a measure for the quality of the fit. In this example, for the model a true TauNorm of 0 was assumed, while for the simulation of the data, a true TauNorm=1 was assumed. The resulting χ^2-histogram shows how sensitive ORCA is concerning ν_τ-appearance (only up-going evens are considered).

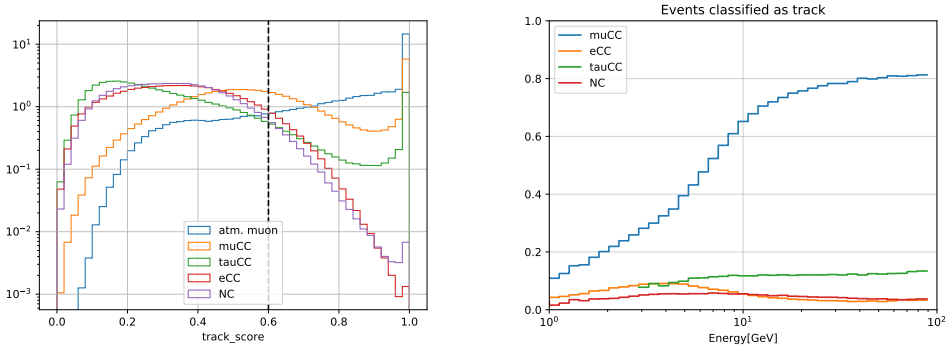

(a) Track-likelihood.

(b) Fraction of events classified as track.

Figure 4.2: Particle Identification (PID) with the RDF. (a) Track-likelihood distribution (normed) from RDF for different event types ($E\epsilon\,[1, 100]$ GeV). Events with track-score > 0.6 are classified as track-like. (b) Fraction of events classified as track per interaction channel. Remember the 17% probability for a τ to decay into a μ (track-event).

4.2 ORCA-115

4.2.1 Event reconstruction and PID

Before the ν_τ-sensitivity can be calculated, the data runs through the steps described in section 3.4. After the event reconstruction and application of selection cuts, all detected events get classified into track- or shower-like.
Figure 4.2 (a) shows the distribution of the track-score (Likelihood to be a track-like event) for different event types. The threshold for an event to be classified as track-like is set to 0.6. This value was chosen empirically and it showed that it has no notable impact if it is changed in the order < 0.1. Looking on the fraction of events that are classified as track (fig. 4.2 (b)) one sees that for higher energies the particle identification (PID) gets more accurate, due to a higher light yield. Also the propagation length of the muon increases, which makes the classification as track easier.

The quality of the event reconstruction can be evaluated by comparing true MC values to reconstruction values. For the analysis of the event reconstruction, all neutrino flavours (CC+NC) are considered. Since SWIM only differs between track- and shower-like events, too, this is a valid proceeding to analyse correlations between the event reconstruction and the results of SWIM. The events are weighted such that the final event rates in the detector are complied, i.e like in section 3.5. This method is kept for all resolution plots in this thesis.
The resolution plots are shown in Figure 4.3 (shower-like) & 4.4 (track-like). The median and 15% & 85%-quantiles of the distribution of the value on the y-axis are drawn. The position and zenith angle resolutions of shower-like events get better at high energies due

to the higher light yield. In the track-channel energy and position resolution shows a different behaviour. Reason for this are high energetic events outside the instrumented volume, where the muon produces enough light inside the detector to trigger an event. The shower-vertex is not seen by the detector and can not be reconstructed, leading to an underestimation of the neutrino energy.
Note that in both reconstructions the reconstructed energy has a non-constant offset relative to the true energy.
Both atmospheric muons and noise contamination are suppressed with a high efficiency by the RDF (noise: $< 1\%$; atmospheric muons: $\sim 1\%$) and neglected in the analysis. The final data sample can now be evaluated for ν_τ-appearance sensitivity studies with SWIM.

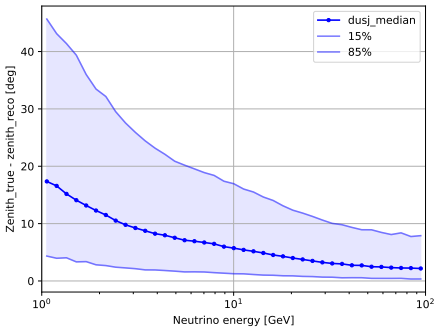

(a) Zenith resolution

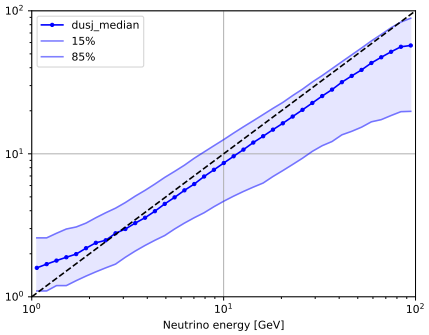

(b) Energy resolution

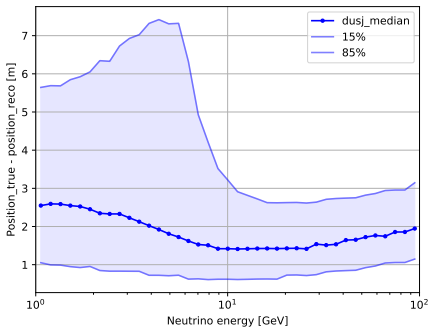

(c) Vertex position resolution

Figure 4.3: Reconstruction of selected **shower-like** neutrino events with Dusj.

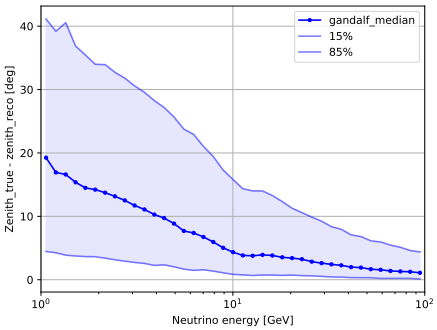

(a) Zenith resolution

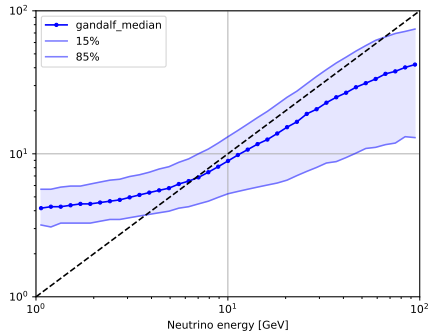

(b) Energy resolution

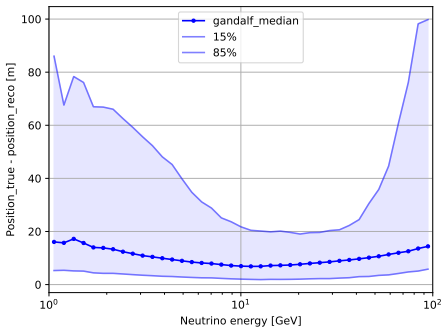

(c) Vertex position resolution

Figure 4.4: Reconstruction of selected **track-like** neutrino events with JGandalf.

Selection criteria are a vertex position inside or near the instrumented volume and a good reconstruction likelihood. All plots have binned x-axes with log10(energy) bins.

4.2.2 Sensitivity studies

The output of SWIM, starting with similar fit parameters used in [33] is shown in Figure 4.5(a). The program finds a minimum of the TauNorm profile at TauNorm = 1, which is expected since this is the true value set in the input. Figure 4.5 shows the output of ten single SWIM runs with different livetimes. After one year of measurement the TauNorm can be restricted to $^{+0.25}_{-0.23}$ with a $3\,\sigma$ C.L. These constraints are in the order of the global limits to the tau-sector introduced in section 2.2. A ν_τ-non-appearance (TauNorm = 0) can be excluded within the first weeks of data-taking. This leads to the assumption, that an early state detector version of ORCA could be already capable to exclude a ν_τ-non-appearance.
Figure A.4 shows, how the final TauNorm profile is composed of the result from the shower- and the track-channel and the errors from the systematics (by quadratic summation). As mentioned before, most ν_τ-events leave a shower-like signature in the detector, which is the reason why the highest contribution comes from the shower-class.
The ν_τ-sensitivity is almost independent of the mass hierarchy. A wrong assumed mass hierarchy leads to an systematic error of $< 5\%$ (fig. A.5). For all presented results, the normal mass ordering was assumed to be true.
Both results are consistent with previous results using ParaNMH (fig. A.6). Yet, for TauNorm > 1, ParaNMH estimates higher sensitivities than SWIM. The reason for this may be the different handling of flux normalisations in both frameworks. SWIM distinguishes between a overall flux normalisation and the ν_τ-normalisation, while in ParaNMH the normalisations of $\nu_{e,\mu,\tau}$CC get fitted, respectively. In the latter case it can thus happen, that the ν_τ-normalisation changes but not the ratio ν_τ- ν_{other}-normalisation. In SWIM this is prevented by the flux normalisation parameter, that can vary the flux of all flavours without changing the ν_τ-normalisation.
The systematics that were used in this analysis are now discussed.

4.2.3 Study of systematics

The expected event rates in the ORCA detector, that are used to calculate its sensitivity to ν_τ-appearance (as explained in section 4.1) are subject to several uncertainties. In addition to the imperfect knowledge of oscillation parameters, this affects especially the atmospheric neutrino flux. Detector and cross section uncertainties are not included in the analysis[1]. All parameters that were used for the calculation of the ν_τ-sensitivity in SWIM are listed in Table 4.1. The upper part of the table contains the oscillation parameters (see subsection 2.1.2). The parameters in the lower part concerns systematics in the neutrino flux:

- **Flux normalisation:** overall normalisation of the atmospheric neutrino flux.

[1] Uncertainties of the ν_τ cross section discussed in subsection 2.1.4 contribute approximately linearly to the systematic error of the TauNorm measurement (see Equation 3.4)

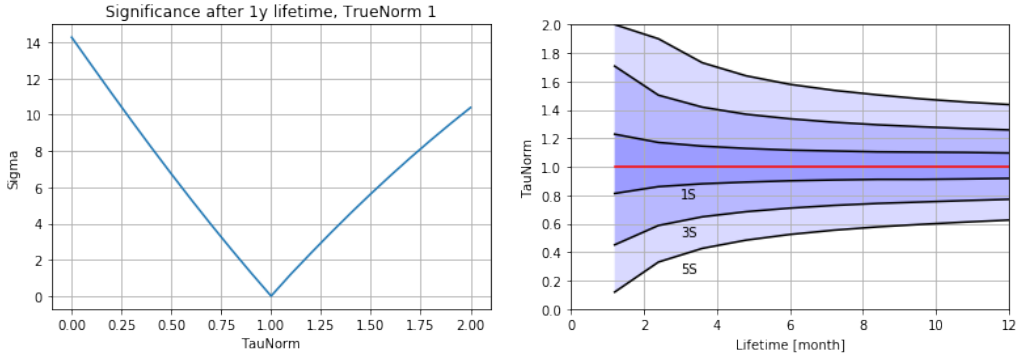

(a) TauNorm exclusion after one year detector lifetime.

(b) TauNorm exclusion over liftetime of detector. Black lines mark the $1\,\sigma$, $3\,\sigma$ and $5\,\sigma$ exclusion significance.

Figure 4.5: ν_τ-appearance sensitivity results of SWIM for the full ORCA detector after one year live-time. For the simulated data true TauNorm = 1 and normal hierarchy were assumed.

- **NC scale:** Scaling of the ratio between CC and NC events (depending on cross sections).
- $\frac{(\nu_\mu+\bar{\nu}_\mu)}{(\nu_e+\bar{\nu}_e)}$**-skew:** Deviation from the ratio between ν_μ and ν_e.
- $\frac{\bar{\nu}_x}{\nu_x}$ **-skew:** Deviation from the ratio between $\bar{\nu}$ and ν.
- **Energy slope:** Deviation from the atmospheric spectral index γ (see Equation 2.14).

The priors are inspired by [23]. Not all parameters have the same impact on the ν_τ-sensitivity. Figure 4.6(a) shows one TauNorm profile for each parameter. For each plot, the parameter stated in the legend was fixed. Most of the results vary only slightly from each other. Two conspicuous results come from a fixed Θ_{23} and NC scale. In the first case, the TauNorm is overestimated (>1). This is due to the fact, that only for Θ_{23} start and true value are different, because of its special treatment in SWIM, i.e. the dual fit with to different start values. Since the "true" value 45% leads to a maximal flavour mixing, the data histogram contains more ν_τ than the model histogram, with less flavour mixing ($\Theta_{23} = 40/50°$).
In the second case, a strong asymmetry for TauNorm $\lessgtr 1$ appears. This becomes apparent in Figure 4.6(b), where the differences of χ^2 values for two TauNorm values $\lessgtr 1$ are plotted. The reason why the NC scale stand out from the other parameters, is the energy-zenith distribution of NC events (fig. 4.7). Although the neutrino leaves the detector again after a NC interaction, it can still transfer most of its energy to the target system. Especially the shower-like NC events have reconstructed energies up to $\sim 30\,\mathrm{GeV}$ and can thus be mistaken as ν_τ. Consequently, a variation of the NC scale has

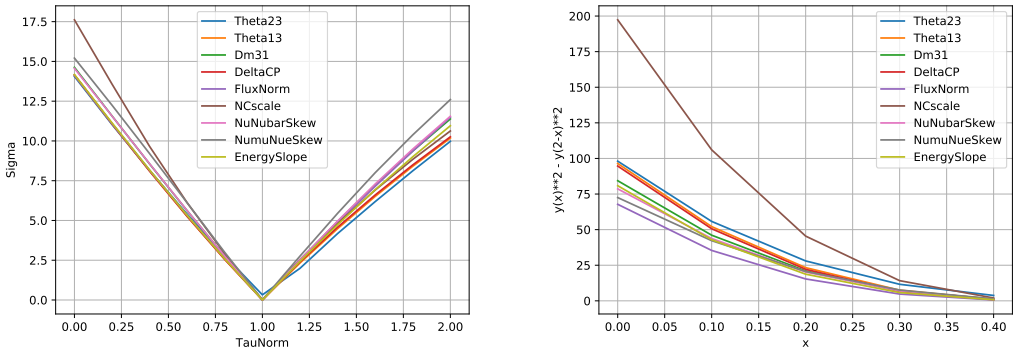

(a) TauNorm profile

(b) Asymmetries

Figure 4.6: Influences of single parameter to SWIM. (a) TauNorm profile for different sets of variable parameters. For each SWIM fit, the written parameter was fixed. The strongest deviation can be observed for a fixed NC scale. (b) Asymmetry of the curves for TauNorm$\lessgtr 1$ in the left plot. It shows that a fixed NC scale results in a high asymmetry between TauNorm$\lessgtr 1$.

a big influence on the ν_τ-sensitivity.
Figure A.9 shows the fit results of each parameter in Table 4.1 for the fixed TauNorm fit (step 3. in 4.1). Here one sees how the individual parameters are varied, in order to compensate the missing (TauNorm<1) or surplus (TauNorm>1) ν_τ-events. As explained before, this happens primary through the variation of the NC scale. In Figure 4.8 one sees that for TauNorm<1 the fit algorithm increases the NC scale significantly (up to $\sim 7\,\sigma$) in order to fill the energy-zenith region in the model histogram, where ν_τ-events are "measured" (data histogram). Similarly, at TauNorm>1 the NC scale is decreased.
The jumps in the fit results occur, if the fit ends in a different local minimum. This is also visible in the fit results of the other parameters, where the jumps appear at the same TauNorm (0.2 and 1.5).
From all fit parameters and systematics, the NC scale was shown to influences the ν_τ-sensitivity the most. A possible solution to reduce the uncertainty caused by the NC scale would be the implementation of a NC analysis. So far, both Swim and ParaNMH only use CC events for their analysis.

4.2.4 Discussion of event selection cuts

The event selection cuts for the 115DU production (see section 3.4) are now discussed and evaluated. It shows that the selected events are reconstructed more precisely than those who are not (A.2&A.3) but the event statistics is reduced by approx. 57%. A comparison between the loose data sample (no selection cuts) with the selected events shows, that

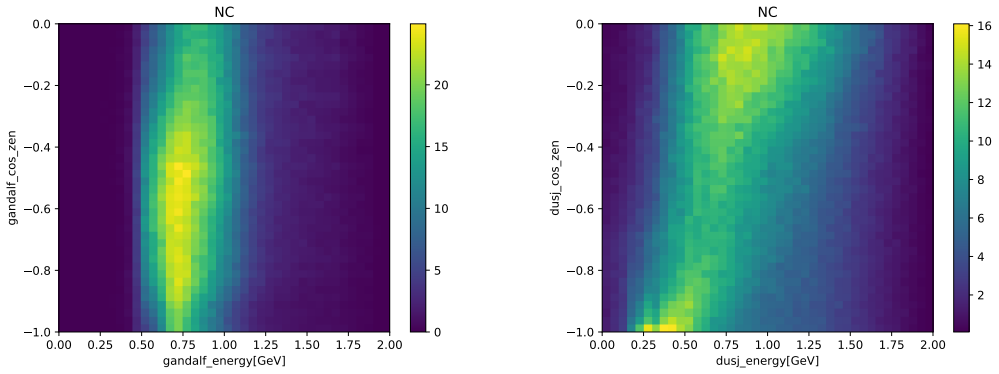

(a) Track-like (b) Shower-like

Figure 4.7: Energy-zenith distribution of NC-events for (a) track-like and (b) shower-like events. The NC-events are reconstructed near the significant region of the ν_τ-sensitivity (fig. 4.15(c)).

the ν_τ-sensitivity worsens only marginally for the reduced data set (fig. 4.9). It is not easy to tell if selection cuts are mandatory for ν_τ-appearance studies with the full ORCA detector, because it exists only a PID output from a training with selected events. The most important question is, if the background suppression would be as efficient as it is without selection cuts before the PID calculation. Yet, the result presented in (fig. 4.9) shows, that the selection cut comes with a negligible disadvantage and can therefore kept without concerns, regarding the accompanying improvements of the resolutions.
Since SWIM allows a variable definition of PID classes, it is a perfect tool for testing selection cuts and their influence to ν_τ-sensitivity. Additional to the already existing cuts, selection criteria based on the start- and end-position of the reconstructed track/shower-event were tested. Figure A.10 shows the reconstruction resolution of track-like events, whose endpoint is reconstructed inside a can with dimensions $r = 150\,\mathrm{m}$ and $h = 100\,\mathrm{m}$ in the centre of the instrumented volume ($\sim 60\%$ of events). Although the resolution of these events is improved, one loses sensitivity to ν_τ-appearance (fig. A.11,weakly constrained). This leads to the assumption, that the major contribution from the selection cuts comes from improvements of the PID. The RDF can distinguish different event types more precisely, if the event reconstruction is efficient.
One can estimate the impact of the PID to the ν_τ-sensitivity, by running SWIM with a perfect PID, i.e. all ν_μCC events are classified as tracks and all ν_eCC and ν_τCC events as showers. This was also tested for a perfect reconstruction and the combination of perfect PID and reconstruction. Figure 4.10 shows the TauNorm profile for all three cases, compared with the realistic PID and reconstruction from the simulations. A perfect event reconstruction would improve the ν_τ-sensitivity significantly, but is technical hard to achieve. It is more likely to improve the PID, e.g. with better selection cuts, which holds potential for an improvement of the ν_τ-sensitivity, too.

Parameter	True value	Prior	Start value
Θ_{13}	8.46°	0.15°	8.46°
Θ_{23}	45°	-	40°/50°
Θ_{12}	33.56°	fixed	fixed
Δm^2_{13}	$2.52 \cdot 10^{-3}$ eV	-	$2.52 \cdot 10^{-3}$ eV
Δm^2_{12}	$7.5 \cdot 10^{-5}$ eV	fixed	fixed
δ_{CP}	0	-	0
Flux normalisation	1	-	1
NC scale	1	0.1	1
$\frac{(\nu_\mu+\bar{\nu}_\mu)}{(\nu_e+\bar{\nu}_e)}$-skew	0	0.05	0
$\frac{\bar{\nu}_x}{\nu_x}$ -skew	0	0.05	0
Energy slope	0	0.05	0

Table 4.1: Fit parameters available in SWIM with true values, start values and 1σ gaussian priors. The upper parameters concern oscillation probabilities, the lower ones normalisation/flux-systematics.

Selection cuts are verified to improve the reconstruction quality of the final data but also tend to reduce statistic significantly. They should therefore used as few as possible. In the case of 115DU the existing selection cuts seem to be sufficient.

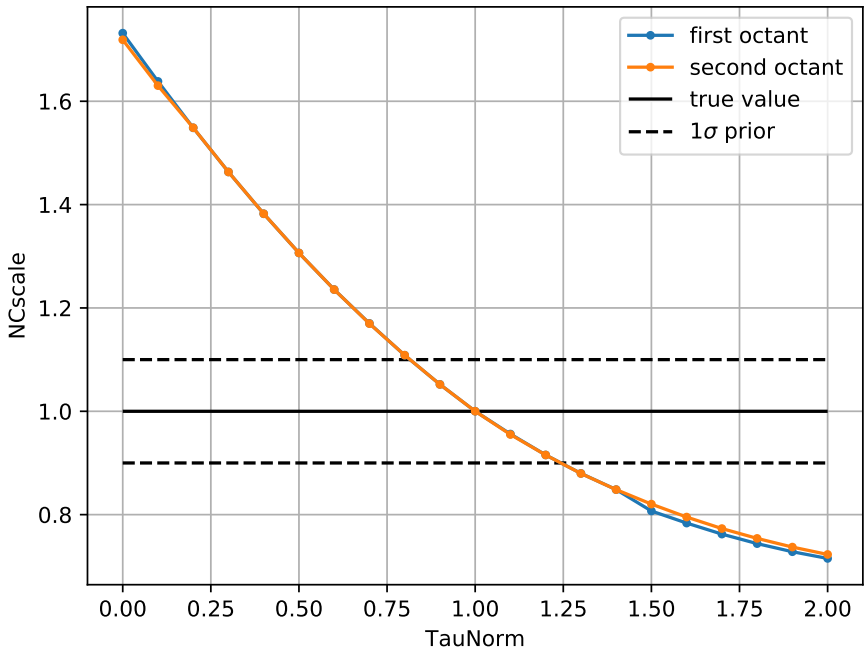

Figure 4.8: Fit results for fixed TauNorm, for both start octants of Θ_{23} (first octant$<$ 45°); second octant$>$ 45°. The true parameter value as well as the 1σ gaussian prior are plotted. Since NC events can mimic ν_τCC-events, this parameter changes significantly over the range of fitted TauNorms (results of other parameters in Figure A.9).

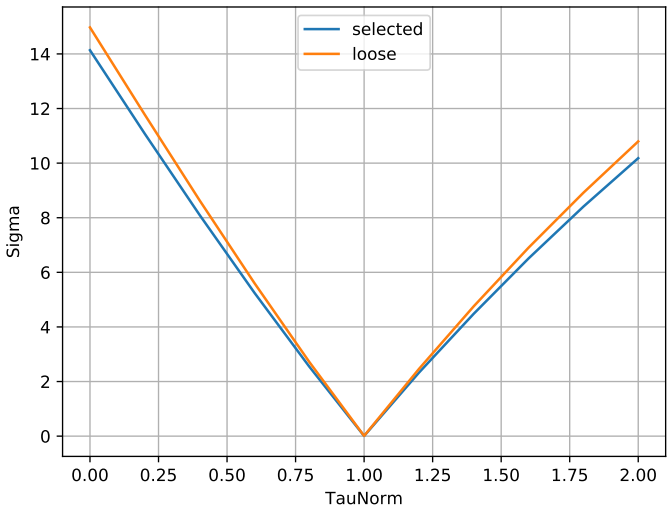

Figure 4.9: TauNorm profile for selected simulated events($\sim$ 111k) and loose selection (selected + deselected: $\sim$ 260k). The data set with applied selection cuts has a slightly worse sensitivity to tau-neutrinos, but a better event reconstruction.

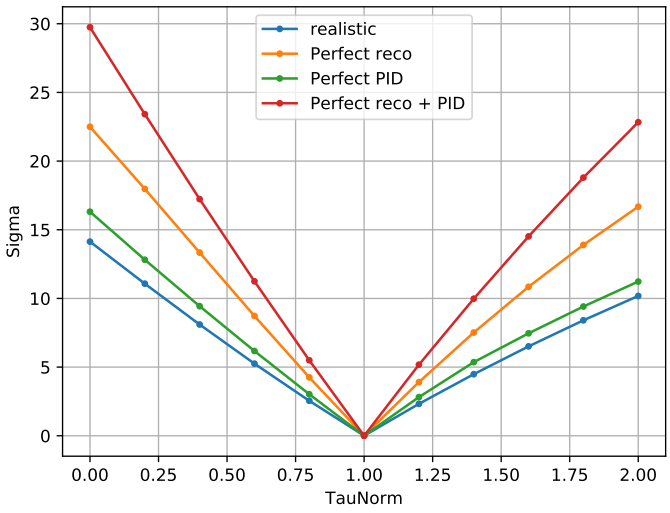

Figure 4.10: TauNorm profile with perfect PID/reconstruction and both combined, compared with realistic PID and reconstruction from simulations.

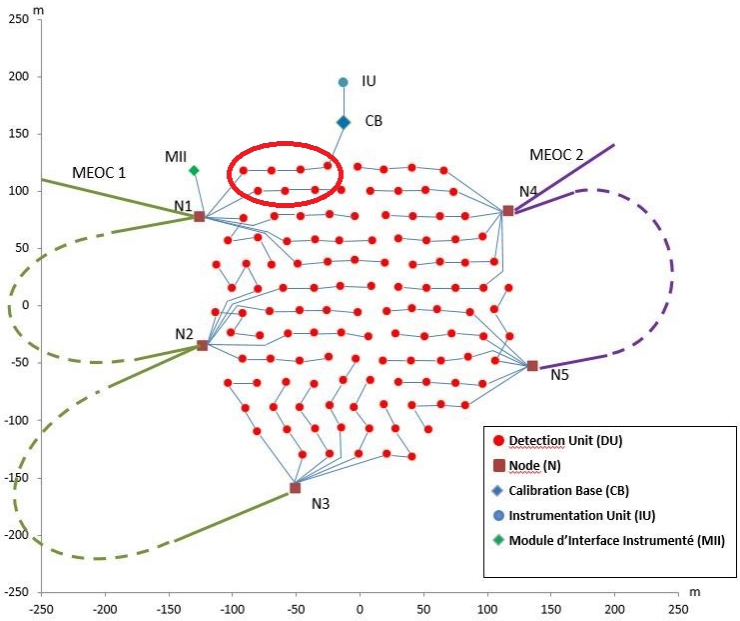

Figure 4.11: ORCA layout with position of strings and electrical infrastructure. The seven lines that were used for the MC are circled in red.

4.3 ORCA-7

In summer 2018, a possible 7-string detector MC was produced. The seven detector lines simulated in this production are marked in Figure 4.11. In this section, all analysis steps from the previous one are applied to this simulation. The event reconstruction and sensitivity to ν_τ-appearance is evaluated. Systematic errors from background events are estimated. For the 7-string data, the only selection criteria for events is, that at least one reconstruction (Dusj or JGandalf) fits an up-going direction. Hence further selection have to be introduced and evaluated. Additionally, possible future improvements are presented.
The effective mass of the 7-string detector is shown in Figure 4.12. These effective masses were calculated without further pre-selection cuts than the up-going condition, and are hence only limitedly comparable with those from the 115-string detector (fig. 3.4).

4.3.1 Event reconstruction and PID

To get a first impression about the performance of the 7-string detector, several basic quantities like energy- & zenith-resolution were determined and compared to the full detector. Figure 4.13 & 4.14 show those quantities versus the true neutrino energy for shower- and track-like neutrino events, respectively. Compared with 115-strings in

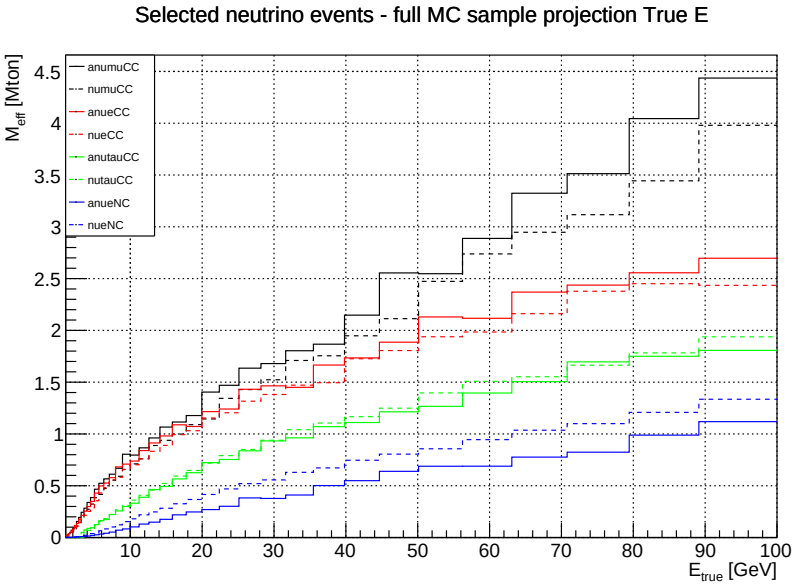

Figure 4.12: Effective mass of the 7-string detector for $\nu/\bar{\nu}$ CC+NC ((a)nueNC stands for all NC events). No pre-selection cuts were used for the calculation.

	115-string		7-string	
	JGandalf	Dusj	JGandalf	Dusj
$\lvert\Delta(E_{85\%}, E_{15\%})\rvert/2E_{\text{median}}$	0.60	0.47	0.62	0.65
$\lvert\Theta_{\text{zenith,true}} - \Theta_{\text{zenith,reco}}\rvert$ [deg]	3.3	4.0	4.4	6.5
$\lvert\text{position}_{\text{true}} - \text{position}_{\text{reco}}\rvert$ [m]	7.6	1.4	11.4	2.4

Table 4.2: Comparison of resolutions for both the 115- and the 7-string detector (Figure 4.3, 4.4, 4.13, 4.14). All values are given for $E_{\nu,\text{true}} = 20\,\text{GeV}$.

section 4.2 the resolutions get worse (Table 4.2). One can recognize the effect described for high-energetic track events in the shower-channel, too. Due to the much smaller instrumented volume it happens more often that a particle shower outside but close to the detector triggers an event. For these events the vertex position is worse than for events starting inside the instrumented volume.
Nevertheless the event reconstruction is sufficient for further analysis. This statement is validated by Figure 4.15. Here all shower-like neutrino events are separated into $\nu_e + \nu_\mu$ and ν_τ-events (CC-only). Although one has significantly less ν_τ-events (note different colorscales) the resulting χ^2 histogram (analogue to Equation 4.1) shows that even with 7 strings one can distinguish between $\overset{(-)}{\nu}_e/\nu_\mu$ and ν_τ on a statistical basis in the $\cos(\Theta_{\text{zenith}})$-energy plane after one year of livetime.
The PID output (fig. 4.16) identifies $\sim 90\%$ of shower events and $\sim 60\%$ (for $E > 10\,\text{GeV}$) of track events correctly.

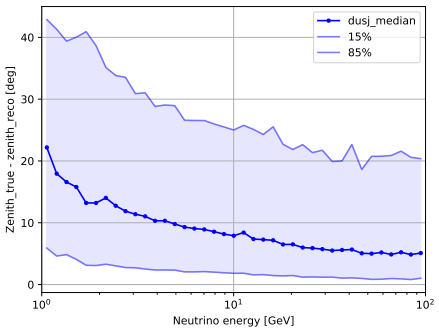

(a) Zenith resolution

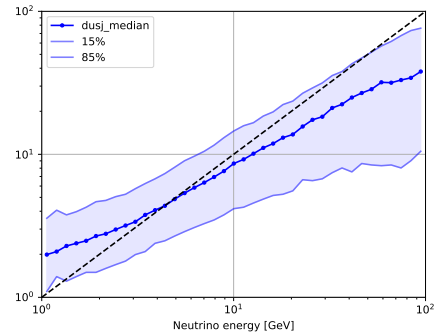

(b) Energy resolution

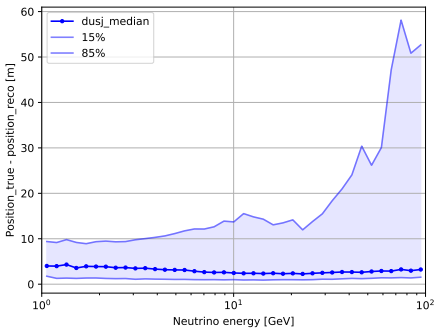

(c) Vertex position resolution

Figure 4.13: Reconstruction of **shower-like** events with Dusj.

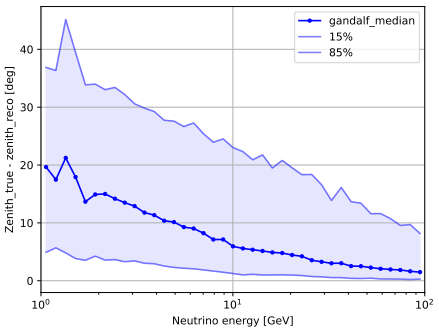

(a) Zenith resolution

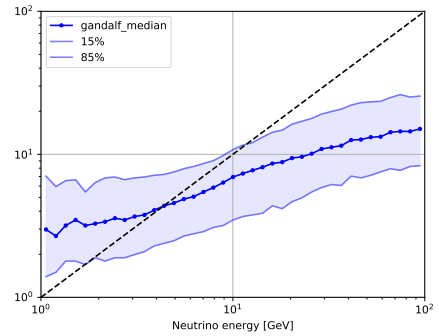

(b) Energy resolution

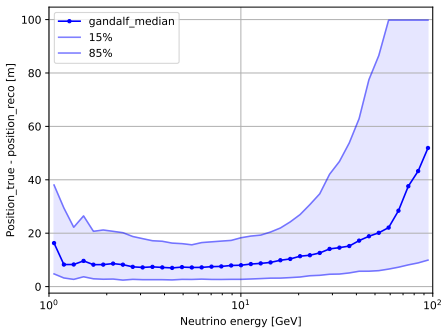

(c) Vertex position resolution

Figure 4.14: Reconstruction of **track-like** events with JGandalf.

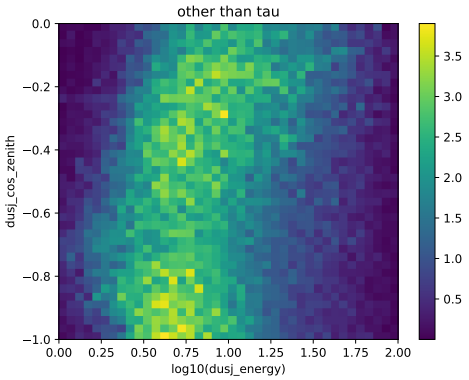

(a) Neutrino events other than ν_τ

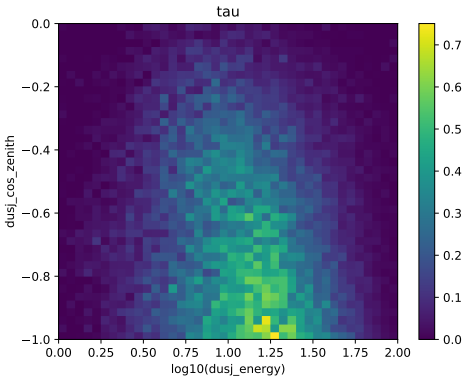

(b) ν_τ-events

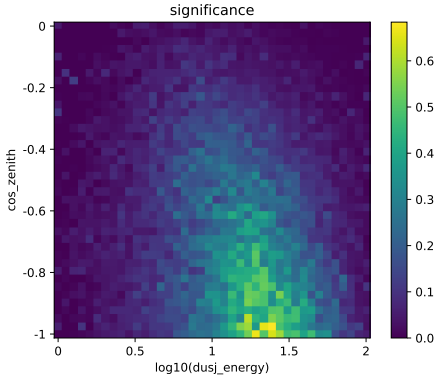

(c) Significance calculated from (a) and (b).

Figure 4.15: Reconstructed shower-like neutrino events split in ν_τ-events(b) and other (a). The resulting significance (c) shows the sensitivitye of ORCA-7 to ν_τ-appearance.

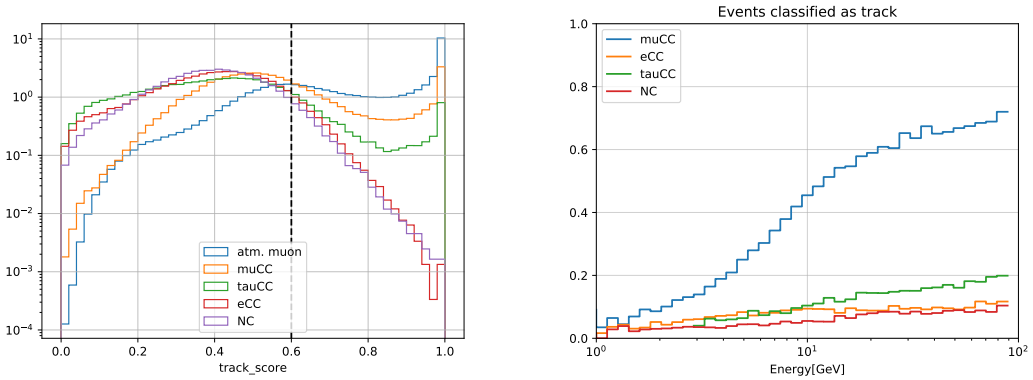

(a) Track-likelihood distribution.

(b) Fraction of events classified as track.

Figure 4.16: Particle Identification (PID) with the RDF in 7-string detector. **(a)** Track-likelihood distribution from RDF for different event types. Events with track-score $>$ 0.6 are classified as track-like. **(b)** Fraction of events classified as track per interaction channel. Remember the 17% probability for a τ to decay into a μ (track-event).

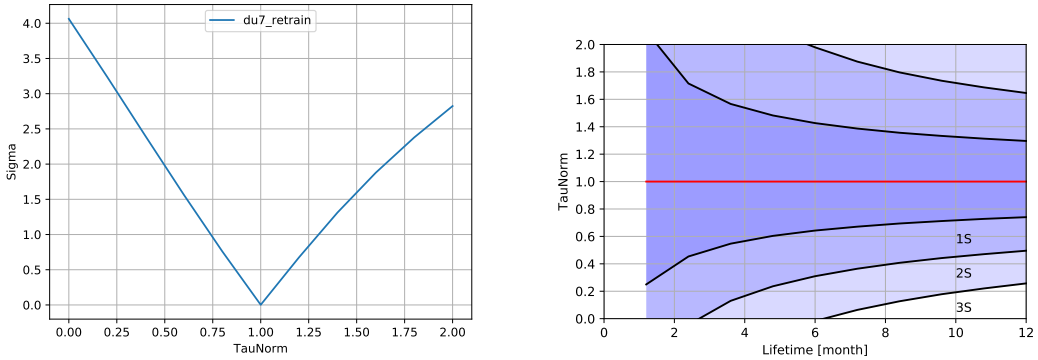

(a) TauNorm exclusion after one year detector live-time.

(b) TauNorm exclusion over livtetime of detector. Black lines mark the 1σ, 3σ and 5σ exclusion significance.

Figure 4.17: Results of SWIM after one year live-time of the 7-string detector. Left: limits on TauNorm of $1^{+0.28}_{-0.26}$ with a 1σ C.L. Right: Exclusion of ν_τ-non-appearance with a 3σ C.L. after ~ 6 months.

4.3.2 Sensitivity studies

The complete procedure for the ν_τ-sensitivity described in the previous chapter can be repeated for the 7-string detector. The first results without any further data processing like selection cuts and without background are shown in Figure 4.17. After one year of livetime one can set limits on the TauNorm of $^{+0.28}_{-0.26}$ with a 1σ C.L. ν_τ-non-appearance can be excluded with a 3σ C.L. after ~ 6 months of livetime.
A similar ν_τ-appearance study with the 8-string IceCube/DeepCore detector [26] results in a TauNorm of $0.57^{+0.36}_{-0.30}$ and an exclusion of ν_τ-non-appearance with $2.0\,\sigma$ after three years of data (CC-only). Although in [26] more systematics are considered, e.g. detector uncertainties and cross-sections, the results of this thesis suggest that a multi-string ORCA array will be able to further constrain the results of IceCube/DeepCore within a year of livetime.

4.3.3 Background events

Noise

With help of the RDF the contamination of noise events in the full detector can be suppressed effectively below 1%. This also works for ORCA-7, reaching a noise contamination of 0.6 $\frac{\text{noise}}{\text{day}}$ vs 33 $\frac{\nu}{\text{day}}$. For one year data-taking the final noise distribution is shown in Figure 4.18. The events are evenly distributed over the zenith angle at mainly low

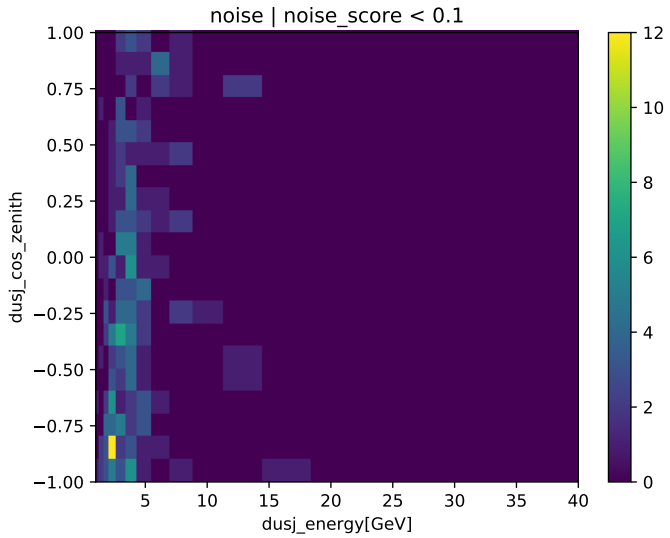

Figure 4.18: Remaining noise events after cut on the noise-score for one a year livetime ($\mathcal{O}(300)$). These events are reconstructed with low energies and over the whole cos-zenith range, and hence not in the significant area for ν_τ-appearance.

energies $< 5\,\text{GeV}$. Compared with Figure 4.15(c) noise seems not to be a problem for ν_τ-appearance measurements, and will be therefore not discussed further in this thesis.

Atmospheric muons

The RDF returns a two dimensional muon-score for the distinction of neutrinos and atmospheric muons. The first dimension comes from a training with a small amount atmospheric muon events. This is sufficient to identify events, that are clearly atmospheric muons, i.e. down-going, high energetic and outside the instrumented volume[2]. For the second dimension, the training uses only atmospheric muon events that are not clearly excluded by the outcome of the first training. As a result the RDF learns to identify atmospheric muons on the basis of finer structures in the data. This proceeding was mandatory, because no pre-selections as described in section 3.4 were available for the 7-string data yet.
The result of 2D-muon-score is shown in Figure 4.19. With a cut on the muon-score, the atmospheric muon contamination can be reduced to 7% with 6000 neutrino events per year remaining. This number is significantly higher than in the 115-string detector ($\sim$ 1%). Thus, the impact of the remaining atmospheric muons on the ν_τ-sensitivity needs to be investigated.

[2]In the 115-string data, these events are filtered out by the selection cuts.

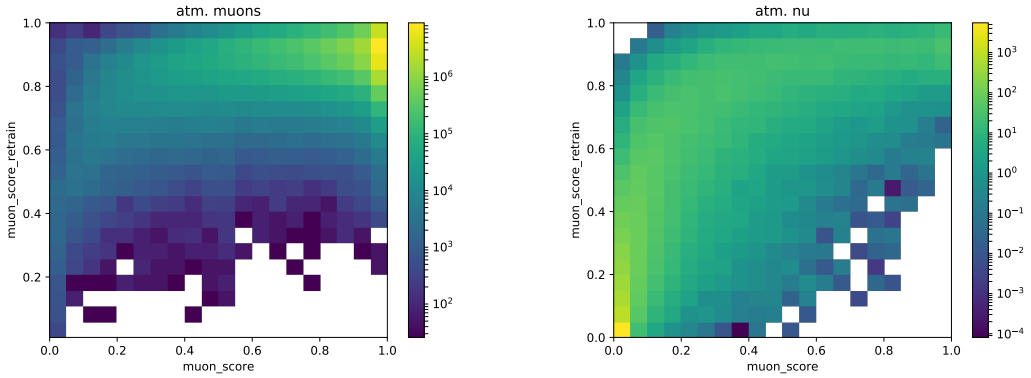

(a) muon-score atmospheric muons

(b) muon-score neutrinos

Figure 4.19: 2D muon-score from the RDF for atmospheric muons (a) and neutrinos (b). Although neutrinos and atmospheric muons are clearly separated, one has to apply very strict cuts on the muon-score, due to the high amount of atmospheric muons (note different colour scales).

SWIM provides a background event class which accounts for atmospheric muons. It is however not trivial to add atmospheric muons to model and data[3], respectively. Due to the high atmospheric muon flux it is very time consuming to simulate, trigger and reconstruct an equivalent number of atmospheric muon events, so only two weeks of atmospheric muon data were simulated. Due to this statistical limitation one can not estimate the atmospheric muon distribution in the final data set after the cut on the muon-score (see fig. 4.20(a)). Therefore SWIM needs a smooth atmospheric muon distribution, created by a loose cut on the atmospheric muon data provided by the user, which is scaled to fit the real atmospheric muon contamination. Possible examples are shown in Figure 4.20(b-d). Picking a loose distribution by hand gives a first impression on the influence of background (fig. 4.21). Neither is the TauNorm fitted wrong, nor suffers the sensitivity for the ν_τ-appearance through the contamination of the remaining atmospheric muons.

A look on the atmospheric muon distributions for individual cuts on the muon score reveals that it is not obvious which loose selection describes to the final muon events while simultaneously providing a smooth distribution in energy and zenith. However, it turned out that the choice of the loose muon distribution has no considerable effect on the TauNorm sensitivity, as long as model and data are identical. Since it is not known how real atmospheric muons will be distributed in energy and zenith, the possibility of a wrongly assumed atmospheric muon model has to be considered[4]. Therefore, a feature

[3] Reminder: the terms model and data refer to the histograms as explained for Figure 4.1.

[4] For the real detector-setup, enough atmospheric muon statistics will be simulated to estimate their reconstructed energy-zenith distribution.

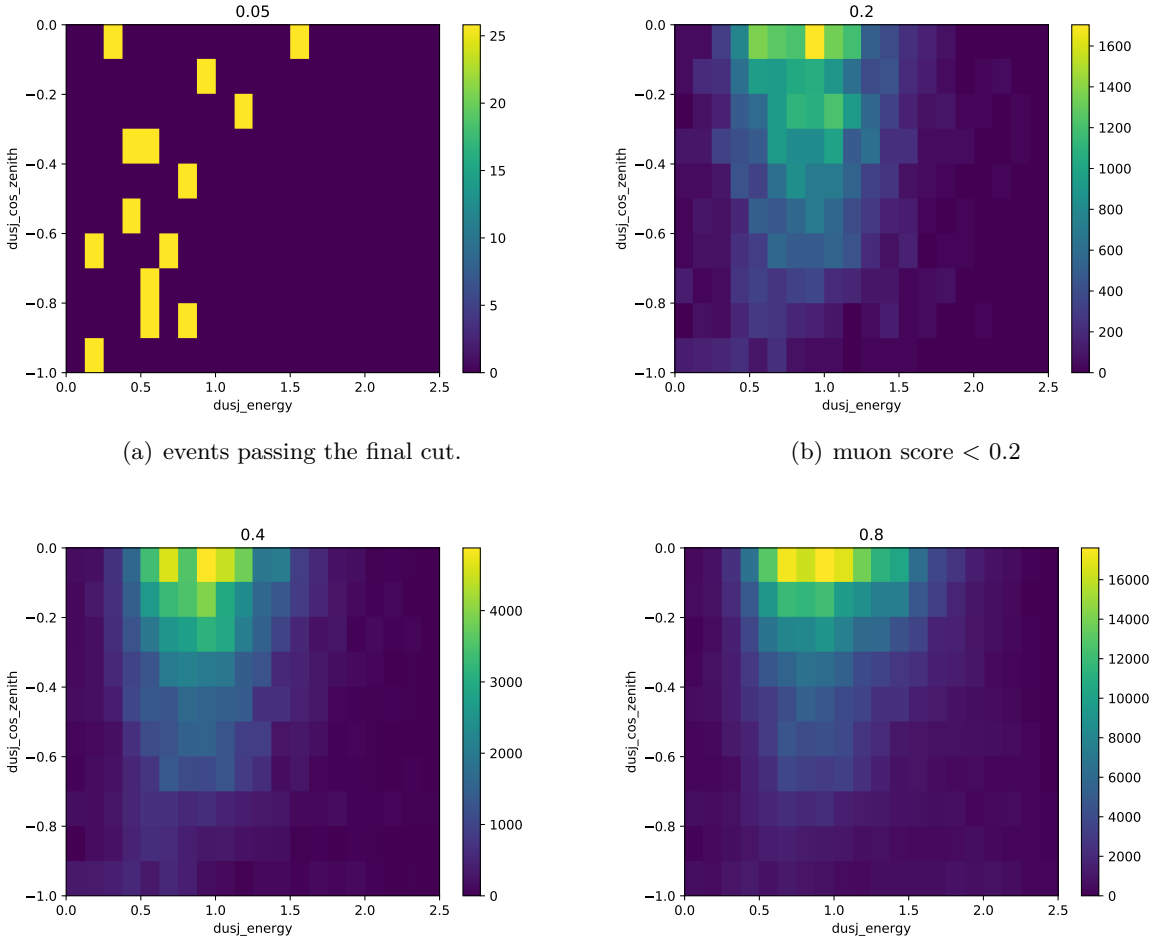

(a) events passing the final cut.

(b) muon score < 0.2

(c) muon score < 0.4

(d) muon score < 0.8

Figure 4.20: Distribution of atmospheric muons after divers cuts on the muon score. (a) is the final cut. (b-d) are possible loose distributions to use for SWIM. Two weeks of atmospheric muon data was simulated.

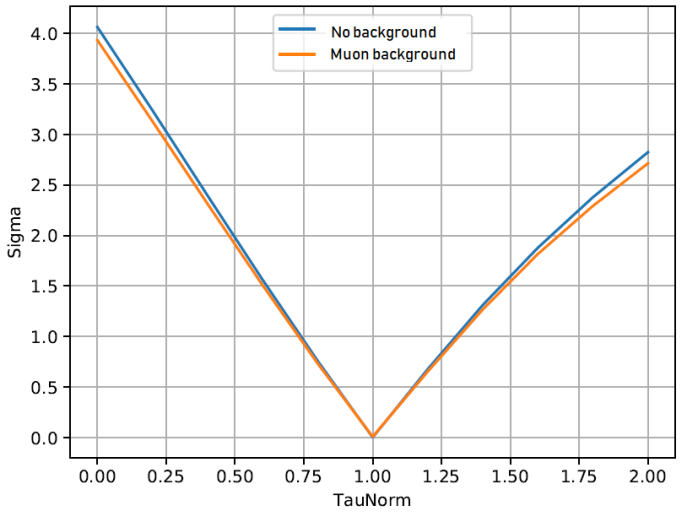

Figure 4.21: 7DU TauNorm profile with and without atmospheric muon background. If the distribution of atmospheric muons in the zenith-energy plane is known, the sensitivity to tau-neutrinos worsens only marginally.

was added to SWIM to add different atmospheric muon distributions for model and data respectively.
To test the new feature on functionality, a worst-case-scenario was investigated: atmospheric muons that are reconstructed as ν_τ (fig. 4.15(b)) while for the model a realistic distribution is assumed (e.g. Figure 4.20(b)). In our case - where the amount n of atmospheric muons and tau-neutrinos is almost equal ($n_\mu \simeq n_{\nu_\tau}$) - the fit finds a minimum at TauNorm $\simeq 2$, since the atmospheric muons are not identified as such, but as ν_τ. The other way around, when atmospheric muons looking like ν_τ are expected (model histogram) but not measured (data histogram), the fit misinterprets half of the ν_τ as atmospheric muons, resulting in a minimum at $\simeq 0.5$ (fig. 4.22).
As we have seen in Figure 4.20, atmospheric muons are not reconstructed near the significant region for the ν_τ-sensitivity (fig. 4.15), as assumed in the described scenarios. A more realistic approach for testing the impact of muon background to the ν_τ-sensitivity is to use realistic, but different atmospheric muon distributions for model and data, respectively. Some examples are shown in Figure 4.23. Again, the outcome of SWIM fits the expectations. Looser cuts in the data with relation to the model means more unexpected muons in the region of ν_τ-excess, resulting in a higher estimated TauNorm. Interchanging data and model leads to an underestimation of the true TauNorm. From those results, a systematic error occurring from a wrongly assumed muon model can be estimated as $\epsilon_{\text{syst}} \leq 15\%$ (fig. 4.23).

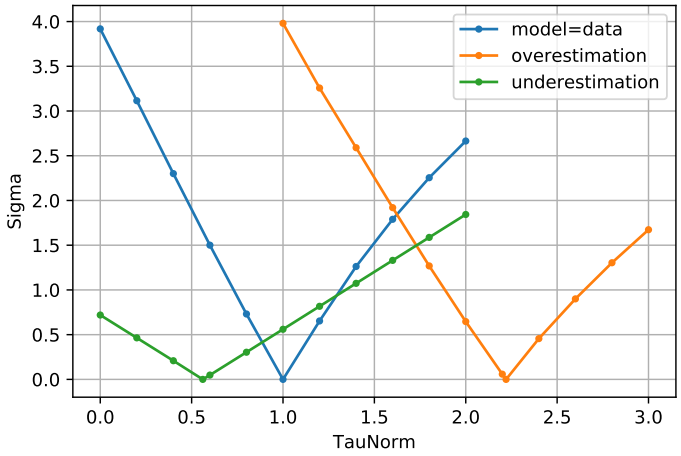

Figure 4.22: TauNormProfile for wrong assumed muon distributions. If the atmospheric muons are reconstructed unexpectedly as ν_τCC-events, the true TauNorm is underestimated (green). If one falsely expects atmospheric muons to be reconstructed as ν_τCC-events, the true TauNorm is overestimated (orange)

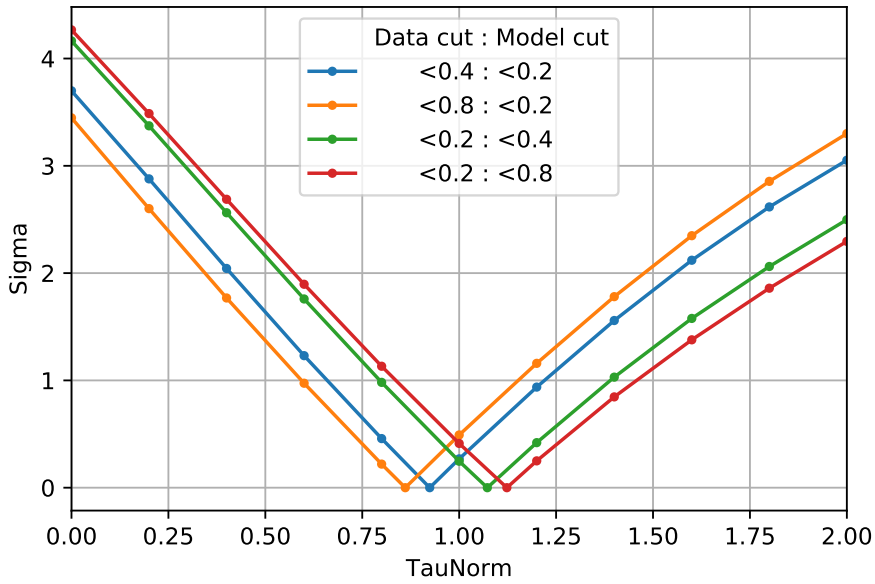

Figure 4.23: TauNorm profile for different atmospheric muon distributions for model and data (see Figure 4.20). True TauNorm $N_{\text{True}} = 1$. The resulting systematic error is $< 15\%$.

4.3.4 Future event selection

As it was discussed in the last chapter, the resolutions and atmospheric muon suppression of the final data sample could be improved by applying additional selection cuts to the data. Some selection cuts can be adapted from the studies of the full ORCA detector without changes, e.g. the demand for a good fit likelihood of Dusj or JGandalf. Other criteria are strongly geometry dependent. For the 7-string detector it seems reasonable to modify these cuts so that they fit to the new detector, i.e. containment cuts and the so called geometric coverage ("GeoCoverage").

Containment

Figure 4.24 shows the reconstructed vertex positions of shower- and track-like neutrino-events in the x-y plane. The red dots mark the positions of the strings, the red ellipse with half-axes $a = 60\,\mathrm{m}$ and $b = 40\,\mathrm{m}$ claims the selected region of events. The dimensions of the ellipse were chosen by hand to include most of the neutrino events while exclude as much atmospheric muon events as possible (see (c)). In z-direction the cuts of the 115-string analysis were kept, since the layout of the single strings does not change.
The fraction of (un-)contained simulated neutrino events can be found in the appendix A.12. Events are deselected evenly over the energy range. Figure 4.25 shows a comparison between the reconstruction quality between track-like[5] neutrino events in- (blue) and outside (red) the selected detector area with clearly better zenith- and position resolution for the contained events. In contrast, the energy resolution worsens for energies above $\sim 10\,\mathrm{GeV}$. Both phenomena may come from muons that are produced inside the detector but end outside. As mentioned in section 4.2, a cut on track events that are completely contained (start and endpoint) is possible, but filters out too many events. Nevertheless it is reasonable to select contained events for the reason that many of the atmospheric muon events are excluded by this cut.
Further optimisations of the containment cuts are possible, e.g. through other can dimensions or different treatment of track- and shower-like events, but were not investigated in the scope of this thesis.

GeoCoverage

The so called GeoCoverage is a quantity used for selection cuts on shower-like events for ORCA, that was introduced in reference [20]. It is the fraction of light beams on a cone with opening angle α, its tip at the vertex and opened alongside the event direction, that lie inside the instrumented volume for a minimum length L_{min} (fig. 4.26(a)). A cut on

[5] Apparently from Figure 4.24(a) nearly all shower-like events are inside the defined volume, which makes a statistical evaluation of non-contained events inadequate. For complementation the analysis can be found in the appendix (Figure A.14).

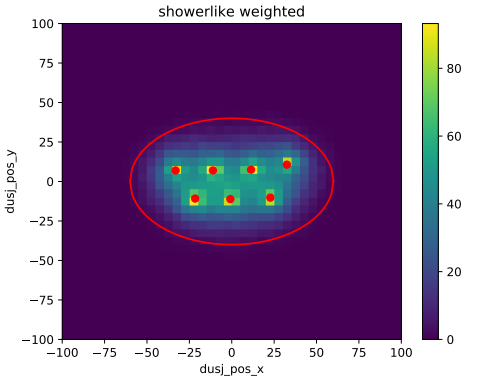

(a) Shower-like events.

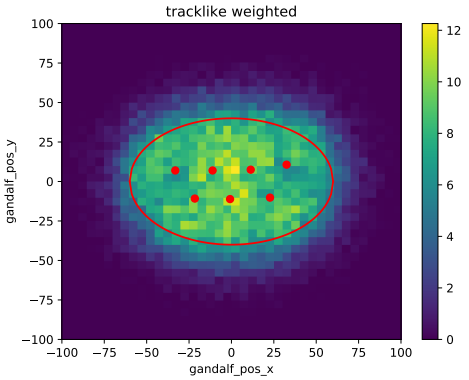

(b) Track-like events.

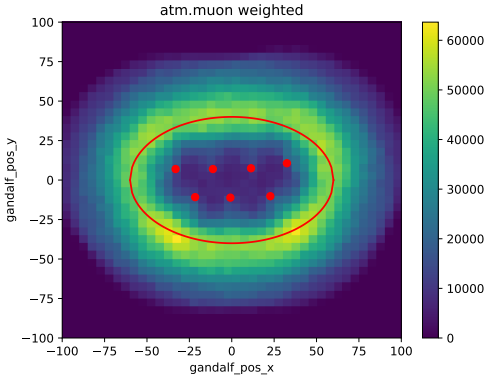

(c) atmospheric muon events.

Figure 4.24: Reco vertex positions in the x-y plane. **(a)&(b)**: neutrino events. **(c)**: atmospheric muons. . Red dots are simulated string positions. Red ellipse shows chosen detector area.

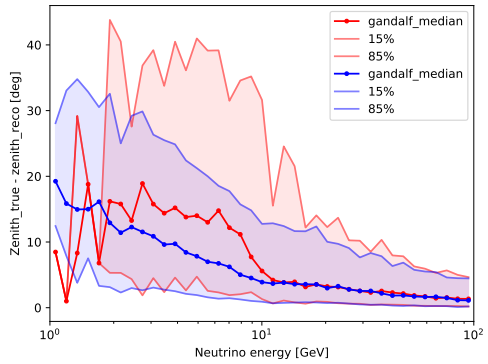

(a) Zenith resolution

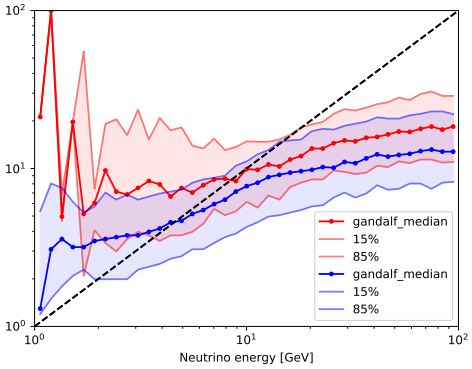

(b) Energy resolution

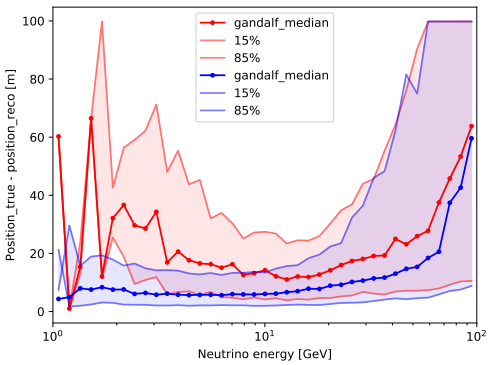

(c) Position resolution

Figure 4.25: Containment: Resolution of selected (blue) vs. deselected (red) **track-like** neutrino events. Note that the deselected statistics for energies $<$ 3 GeV are insufficient.

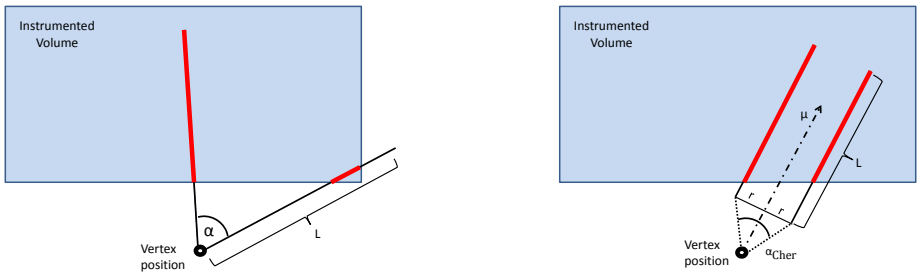

(a) Shower events.

(b) Track events.

Figure 4.26: 2D-scheme of GeoCoverage. **(a)** GeoCoverage for shower events: The fraction of vectors on a cone around the vertex position that lies in the instr. volume, for various opening angles α. **(b)** GeoCoverage for track events: The fraction of vectors on a cylinder around the muon trajectory that lies in the instr. volume, for various radii r.

this value should ensure that a majority of the produced Cherenkov light is contained in the instrumented volume. For the full detector $L_{\text{min}} = 30\,\text{m}$ and $\alpha\,\epsilon\,[20°, 45°, 60°, 75°]$ was chosen. Additionally, the light beam was only tested for coverage for distances $l\,\epsilon\,[10\,\text{m} : 70\,\text{m}]$ from the vertex (attenuation length of Cherenkov light in water $\sim 70\,\text{m}$) [35]. For the much smaller 7-string detector L_{min} was set to 1 m. Figure 4.27 shows the resolutions for shower-like events with a GeoCoverage > 0.4 (selected) and $\leqq 0.4$ (deselected). Only the position resolution shows a slight improvement.
A similar approach was done for track-like events. In contrast to shower-like events with a point-source like light pattern, the Cherenkov light of a track event is produced alongside the trajectory of the μ. Therefore the geometry of the light beams evaluated for the GeoCoverage changes for track-like events (Figure 4.26(b)). Instead of lying on a cone around the vertex position, the tested vectors form the surface of a cylinder with radius r around the reconstructed direction vector of the event. The bottom of the cylinder is shifted by $r \cdot \tan(\Theta_{\text{cher}})$ away from the vertex position, because the Cherenkov light is radiated in an angle of $\Theta_{\text{cher}} = 42°$. The length of the cylinder is the reconstructed track-length.
The GeoCoverage condition for track events is fulfilled if >90% on average ($r\,\epsilon\,[5\,\text{m}, 10\,\text{m}, 15\,\text{m}]$) of the tested vectors are inside the detector volume defined in the section above. Although this strict cut deselects nearly half of the simulated neutrino events (fig. A.13), it ensures a rather good reconstruction of track-like events (fig. 4.28). This can help the RDF to distinguish between atmospheric muons and ν_μCC events in the future.

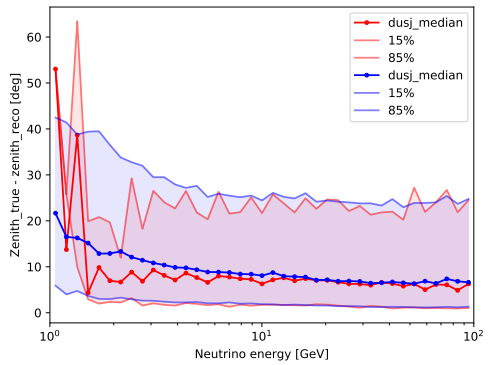

(a) Zenith resolution

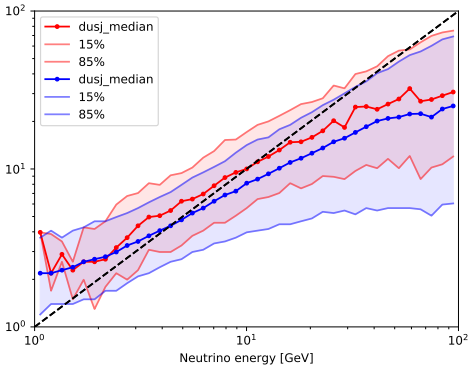

(b) Energy resolution

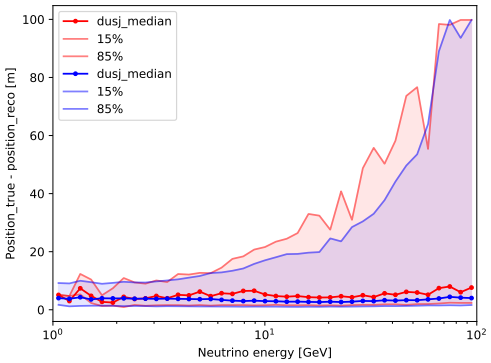

(c) Position resolution

Figure 4.27: GeoCoverage: Resolution of selected (blue) vs. deselected (red) **shower-like** neutrino events.

The containment and GeoCoverage conditions allows to create new selection cuts for the 7-string data. It is reasonable to request every event to have either a good track- or shower-resolution, i.e. containment **and** GeoCoverage are fulfilled for either JGandalf **or** Dusj. This holds true for $\sim 75\%$ of the neutrino events and only $\sim 13\%$ of atmospheric muons. Comparing neutrino events that pass this criteria with the total (unfiltered) data sample, one sees a slight improvement in the event reconstruction (fig. 4.29 & 4.30).
In the future, these selection cuts may be able to improve the PID. Since the worst reconstructed events that are the hardest to identify are pre-selected, the RDF will be more sensitive to fine differences between the event types. A better separation between shower- and track-like seems to be one of the most promising ways to improve the ν_τ-sensitivity. One can test the result of the 7-string detector for a perfect PID (analogue to 115 strings in Figure 4.10). The significance for a ν_τ-non-appearance rises by $\sim 50\%$ (fig. 4.31).

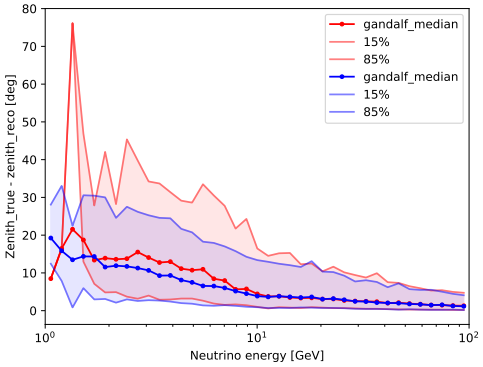

(a) Zenith resolution

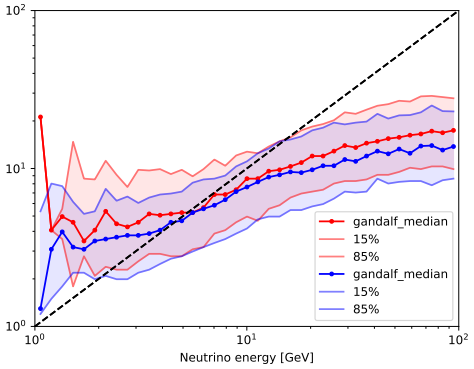

(b) Energy resolution

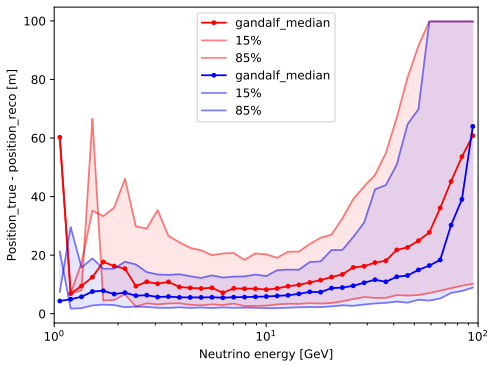

(c) Position resolution

Figure 4.28: GeoCoverage: Resolution of selected (blue) vs. deselected (red) **tracklike** neutrino events.

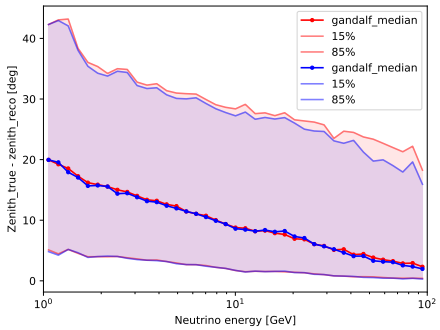

(a) Zenith resolution

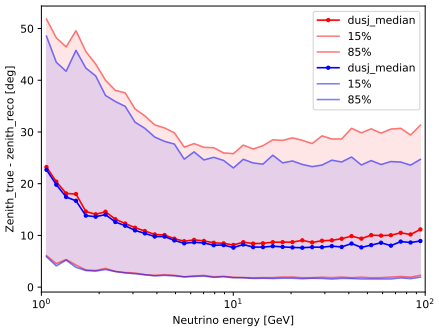

(a) Zenith resolution

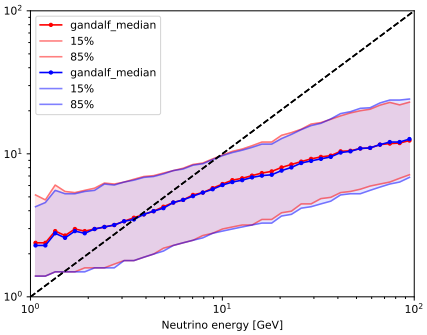

(b) Energy resolution

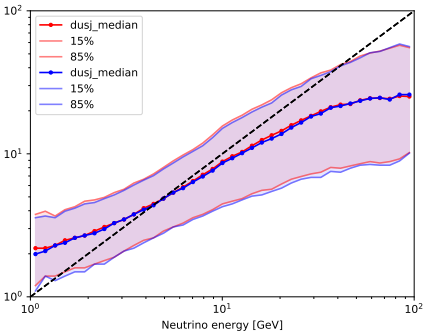

(b) Energy resolution

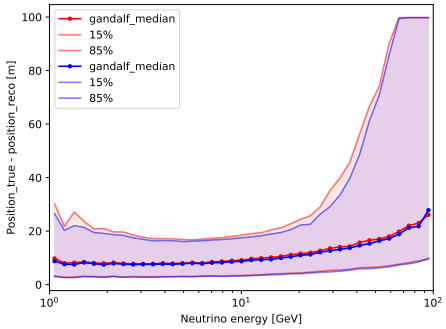

(c) Position resolution

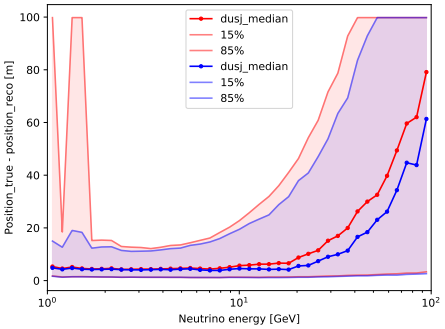

(c) Position resolution

Figure 4.29: Resolution of selected (blue) vs. deselected (red) **track-like** neutrino events in ORCA7.

Figure 4.30: Resolution of selected (blue) vs. deselected (red) **shower-like** neutrino events in ORCA7.

Events are selected, if either for JGandalf or Dusj both containment and GeoCoverage criteria are fulfilled.

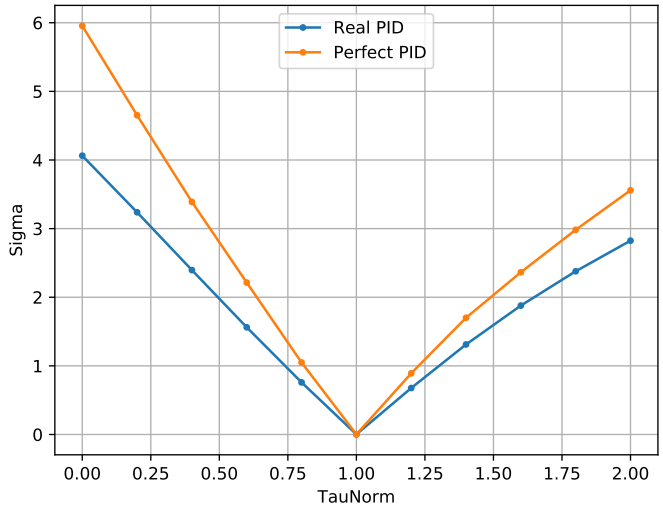

Figure 4.31: TauNorm profile for 7-strings with realistic and perfect PID. The significance for a ν_τ-non-appearance rises by $\sim 50\%$.

4.4 Potential toward PMNS unitarity confirmation

As it was motivated in subsection 2.2.2, measurements of the ν_τ-normalisation in the atmospheric neutrino flux could be used to test the unitarity of the PMNS matrix (Equation 2.1). The direct way to do this is to determine the squared sum of the tau-sector entries in the PMNS matrix (2.16). Since the main contribution of ν_τ in ORCA comes from $\nu_\mu \rightarrow \nu_\tau$ oscillations, ORCA is mainly sensitive to the oscillation parameters Θ_{23} and $|\Delta m^2_{23}|$, thus $|U_{\mu 3}|^2$ and $|U_{\tau 3}|^2$. The results of ORCA could consequently contribute to global fits of the PMNS matrix and its unitarity in combination with results from other experiments.
The potential to test the PMNS unitarity from ORCA's ν_τ-appearance studies alone is limited by uncertainties of the ν_τ cross section (see subsection 2.1.4), because the ν_τ-normalisation is a product of neutrino flux, oscillation probabilities and neutrino cross sections[6]. The theoretical uncertainties of the neutrino cross sections are of the order $\mathcal{O}(10\%)$ and hence in the same order as the errors on the ν_τ-normalisation in the full ORCA detector after one year livetime. Assuming unitarity of the PMNS matrix, the errors on the oscillation probabilities are smaller than those of the cross section [1][28]. If the measured ν_τ-normalisation deviates $\gg \mathcal{O}(10\%)$ from the expected value assuming PMNS unitarity, this would be a strong hint towards physics beyond the standard model. With increasing livetime, the error on the ν_τ-normalisation becomes even smaller (see fig. 4.5(b)). However this will not improve the sensitivity towards the PMNS unitarity, unless the cross section uncertainties get smaller, e.g. by new theoretical models. On the other hand, tighter restrictions of the ν_τ-normalisation enable studies of the ν_τCC cross section, as in [17] from SuperKamiokande.
The ν_τ-normalisation error in the 7-string ORCA detector after one year livetime are in the order $\mathcal{O}(25\%)$ and thus less dominated by the cross section uncertainties.
Not included in the analysis of this thesis are uncertainties in the detector model, e.g. imperfect knowledge of DOM positions due to the sea current, or optical properties, like inhomogeneities of the seawater. Both effects were investigated in the ANTARES project, that uses a similar infrastructure as ORCA, and were found to have negligible effects on the event reconstruction.

[6] Uncertainties in the atmospheric neutrino flux originate mostly from erros of neutrino cross sections[36]

5 Conclusion

The KM3NeT/ORCA detector can contribute to fundamental results in the field of particle physics in the future. One of these outcomes will be the detection of ν_τ in the atmospheric neutrino flux, a direct proof of neutrino oscillations. This allows to test the ν_τ-flux on deviations from the expectations that are dictated by the 3-neutrino framework. The measurement of the ν_τ-normalisation ($= \nu_{\text{Flux}} \cdot \text{oscillation probability} \cdot \text{cross section}$) could tighten the limits on the weakly bounded oscillation parameters in the tau sector of the PMNS-matrix. Yet one has to keep in mind, that deviations from the expected ν_τ-normalisation could not only origin from oscillation parameters but from neutrino cross sections.
Sensitivity studies indicate that the complete ORCA detector can restrict the ν_τ-normalisation to $^{+0.25}_{-0.23}$ at $3\,\sigma$ C.L. with only one year of livetime. The best global fit reaches a $3\,\sigma$ C.L. of $1^{+0.24}_{-0.44}$. Previous analyses concerning the sensitivity to ν_τ-appearance with the ORCA detector could be reproduced using a different analysis framework, which is an independent confirmation of the expected physics potential of the experiment.
With the forthcoming commissioning of a multi-string detector first data will be available soon. The analysis of Monte Carlo data of a possible 7-string detector revealed, that such a small version of ORCA is already capable of gathering enough data for event reconstruction and particle identification. ν_τ-non-appearance can be excluded after 6 months with a $3\,\sigma$ C.L. The ν_τ-normalisation can be restricted to $^{+0.28}_{-0.26}$ with a $1\,\sigma$ C.L. after one year of livetime. These limits are comparable with the recent publication of the IceCube/DeepCore experiment [26], where a similar analysis was used with three years of detector livetime. This is a clear evidence for the competitiveness of ORCA.
Several quality conditions are introduced to deselect badly reconstructed events and ensure the credibility of these results. Some of these selection cuts were adopted from former works, others were defined or had to be adapted to the new geometry of the 7-string detector. Although this leads to lower statistics at first, in the future the particle identification may be improved due to better reconstructed events, which will lead to a net improvement of the sensitivity up to 50%.
Finally, an error to the ν_τ-normalisation sensitivity occurring from the non-negligible contamination of atmospheric muons in the 7-string detector could be estimated. If the reconstructed energy-zenith distribution of atmospheric muons is known, the resulting error is insignificant. Currently, there are not enough simulated atmospheric muon events available for estimating their energy-zenith distribution in the final data, which leads to a systematic error of $\leq 15\,\%$. Again, this error may be reduced by a better particle

identification, i.e. through the exclusion of atmospheric muons in the data.
The conclusion that can be drawn from this thesis is that even a few detection strings of ORCA bear a high potential for neutrino physics. The first ν_τ-appearance studies will be available even before the full ORCA detector is completed. This is a strong signal to other neutrino experiments around the globe and raises hope to outstanding physics for the forthcoming years of ORCA.

6 Bibliography

[1] M. Tanabashi et al. “Review of Particle Physics”. In: *Phys. Rev. D* 98 (3 2018), p. 030001. DOI: 10.1103/PhysRevD.98.030001. URL: https://link.aps.org/doi/10.1103/PhysRevD.98.030001.

[2] K. Abe et al. “Measurement of Atmospheric Neutrino Flux Consistent with Tau Neutrino Appearance”. In: *Phys. Rev. Lett.* 97 (17 2006), p. 171801. DOI: 10.1103/PhysRevLett.97.171801. URL: https://link.aps.org/doi/10.1103/PhysRevLett.97.171801.

[3] Trovato, A. and on behalf of the ANTARES Collaboration. “Recent results from ANTARES”. In: *EPJ Web of Conferences* 99 (2015), p. 06003. DOI: 10.1051/epjconf/20159906003. URL: https://doi.org/10.1051/epjconf/20159906003.

[4] M. G. Aartsen et al. “The IceCube Neutrino Observatory Part V: Neutrino Oscillations and Supernova Searches”. In: *Proceedings, 33rd International Cosmic Ray Conference (ICRC2013): Rio de Janeiro, Brazil, July 2-9, 2013*. 2013. arXiv: 1309.7008 [astro-ph.HE].

[5] N. Schmitz. *Neutrinophysik*. 1997.

[6] S. Mele. “Precision electroweak measurements on the Z resonance”. In: *Physics Reports* 427.5 (2006), pp. 257 –454. ISSN: 0370-1573. DOI: https://doi.org/10.1016/j.physrep.2005.12.006. URL: http://www.sciencedirect.com/science/article/pii/S0370157305005119.

[7] R. Davis. “A review of the homestake solar neutrino experiment”. In: *Progress in Particle and Nuclear Physics* 32 (1994), pp. 13 –32. ISSN: 0146-6410. DOI: https://doi.org/10.1016/0146-6410(94)90004-3. URL: http://www.sciencedirect.com/science/article/pii/0146641094900043.

[8] K. S. Hirata et al. “Observation of B-8 Solar Neutrinos in the Kamiokande-II Detector”. In: *Phys. Rev. Lett.* 63 (1989), p. 16. DOI: 10.1103/PhysRevLett.63.16.

[9] J. Abdurashitov et al. “Results from SAGE (The Russian-American gallium solar neutrino experiment)”. In: *Physics Letters B* 328.1 (1994), pp. 234 –248. ISSN: 0370-2693. DOI: https://doi.org/10.1016/0370-2693(94)90454-5. URL: http://www.sciencedirect.com/science/article/pii/0370269394904545.

[10] T. Kirsten. “GALLEX solar neutrino results”. In: *Progress in Particle and Nuclear Physics* 40 (1998). Neutrinos in Astro, Particle and Nuclear Physics, pp. 85 –99. ISSN: 0146-6410. DOI: https://doi.org/10.1016/S0146-6410(98)00013-1. URL: http://www.sciencedirect.com/science/article/pii/S0146641098000131.

[11] C. Giganti, S. Lavignac, and M. Zito. “Neutrino oscillations: The rise of the PMNS paradigm”. In: *Progress in Particle and Nuclear Physics* 98 (2018), pp. 1 –54. ISSN: 0146-6410. DOI: https://doi.org/10.1016/j.ppnp.2017.10.001. URL: http://www.sciencedirect.com/science/article/pii/S014664101730087X.

[12] F. An and ohters. “Neutrino physics with JUNO”. In: *Journal of Physics G: Nuclear and Particle Physics* 43.3 (2016), p. 030401. DOI: 10.1088/0954-3899/43/3/030401. URL: https://doi.org/10.1088%2F0954-3899%2F43%2F3%2F030401.

[13] S. Mikheyev and A. Smirnov. “Resonant neutrino oscillations in matter”. In: *Progress in Particle and Nuclear Physics* 23 (1989), pp. 41 –136. ISSN: 0146-6410. DOI: https://doi.org/10.1016/0146-6410(89)90008-2. URL: http://www.sciencedirect.com/science/article/pii/0146641089900082.

[14] A. M. Dziewonski and D. L. Anderson. “Preliminary reference Earth model”. In: *Physics of the Earth and Planetary Interiors* 25.4 (1981), pp. 297 –356. ISSN: 0031-9201. DOI: https://doi.org/10.1016/0031-9201(81)90046-7. URL: http://www.sciencedirect.com/science/article/pii/0031920181900467.

[15] J. A. Formaggio and G. P. Zeller. “From eV to EeV: Neutrino cross sections across energy scales”. In: *Rev. Mod. Phys.* 84 (3 2012), pp. 1307–1341. DOI: 10.1103/RevModPhys.84.1307. URL: https://link.aps.org/doi/10.1103/RevModPhys.84.1307.

[16] K. Kodama and ohters. “Final tau-neutrino results from the DONuT experiment”. In: *Phys. Rev. D* 78 (5 2008), p. 052002. DOI: 10.1103/PhysRevD.78.052002. URL: https://link.aps.org/doi/10.1103/PhysRevD.78.052002.

[17] Z. Li et al. “Measurement of the tau neutrino cross section in atmospheric neutrino oscillations with Super-Kamiokande”. In: *Phys. Rev. D* 98 (5 2018), p. 052006. DOI: 10.1103/PhysRevD.98.052006. URL: https://link.aps.org/doi/10.1103/PhysRevD.98.052006.

[18] Y. S. Jeong and M. H. Reno. “Tau neutrino and antineutrino cross sections”. In: *Phys. Rev. D* 82 (3 2010), p. 033010. DOI: 10.1103/PhysRevD.82.033010. URL: https://link.aps.org/doi/10.1103/PhysRevD.82.033010.

[19] L. Pasquali and M. H. Reno. “Tau neutrino fluxes from atmospheric charm”. In: *Phys. Rev. D* 59 (9 1999), p. 093003. DOI: 10.1103/PhysRevD.59.093003. URL: https://link.aps.org/doi/10.1103/PhysRevD.59.093003.

[20] J. Hofestädt. “Measuring the neutrino mass hierarchy with the future KM3NeT/ORCA detector”. PhD Thesis. Friedrich-Alexander-Universität Erlangen, ECAP, 2017.

[21] T. K. Gaisser and M. Honda. “Flux of atmospheric neutrinos”. In: *Annual Review of Nuclear and Particle Science* 52.1 (2002), pp. 153–199. DOI: 10.1146/annurev.nucl.52.050102.090645. eprint: https://doi.org/10.1146/annurev.nucl.52.050102.090645. URL: https://doi.org/10.1146/annurev.nucl.52.050102.090645.

[22] M. Honda et al. “Atmospheric neutrino flux calculation using the NRLMSISE-00 atmospheric model”. In: *Phys. Rev. D* 92 (2 2015), p. 023004. DOI: 10.1103/PhysRevD.92.023004. URL: https://link.aps.org/doi/10.1103/PhysRevD.92.023004.

[23] S. Adrián-Martinéz et al. “Letter of intent for KM3NeT 2.0”. In: *Journal of Physics G: Nuclear and Particle Physics* (2016).

[24] N. Agafonova et al. “Observation of a first nutau candidate event in the OPERA experiment in the CNGS beam”. In: *Physics Letters B* 691.3 (2010), pp. 138 –145. ISSN: 0370-2693. DOI: https://doi.org/10.1016/j.physletb.2010.06.022. URL: http://www.sciencedirect.com/science/article/pii/S0370269310007537.

[25] N. Agafonova and ohters. “Final Results of the OPERA Experiment on ν_τ Appearance in the CNGS Neutrino Beam”. In: *Phys. Rev. Lett.* 120 (21 2018), p. 211801. DOI: 10.1103/PhysRevLett.120.211801. URL: https://link.aps.org/doi/10.1103/PhysRevLett.120.211801.

[26] M. G Aartsen et al. “Measurement of atmospheric tau neutrino appearance with IceCube DeepCore”. In: *Phys. Rev. D* 99 (3 2019), p. 032007. DOI: 10.1103/PhysRevD.99.032007. URL: https://link.aps.org/doi/10.1103/PhysRevD.99.032007.

[27] X. Qian et al. “Unitarity tests of the neutrino mixing matrix”. In: 2013. arXiv: 1308.5700.

[28] S. Parke and M. Ross-Lonergan. “Unitarity and the three flavor neutrino mixing matrix”. In: *Phys. Rev. D* 93 (11 2016), p. 113009. DOI: 10.1103/PhysRevD.93.113009. URL: https://link.aps.org/doi/10.1103/PhysRevD.93.113009.

[29] P. A. Čerenkov. “Visible Radiation Produced by Electrons Moving in a Medium with Velocities Exceeding that of Light”. In: *Phys. Rev.* 52 (4 1937), pp. 378–379. DOI: 10.1103/PhysRev.52.378. URL: https://link.aps.org/doi/10.1103/PhysRev.52.378.

[30] T. Eberl. *Neutrinophysik lecture*. Friedrich-Alexander-Universität Erlangen. 2018.

[31] D. Stransky et al. “Reconstruction of cascade-type neutrino events in KM3NeT/ARCA”. In: *Proc. 34th Int. Cosmic Ray Conference*. Vol. 001, 1114. 2015.

[32] A. Trovato et al. “Muon track reconstruction and muon energy estimate in the KM3NeT/ARCA detector”. In: *Proc. 34th Int. Cosmic Ray Conference*. Vol. 001, 1106. 2015.

[33] T. Eberl, S. Hallmann, and J. Hofestädt. “Tau neutrino appearance with KM3NeT/ORCA”. In: Aug. 2017, p. 1025. DOI: 10.22323/1.301.1025.

[34] S. Bourret. “Neutrino oscillations and Earth tomography with KM3NeT-ORCA”. PhD Thesis. Université Paris Diderot, 2019.

[35] A. Margiotta. "Systematic uncertainties in Monte Carlo simulations of the atmospheric muon flux in the 5-line ANTARES detector". In: *Nuclear Instruments and Methods in Physics Research Section A: Accelerators, Spectrometers, Detectors and Associated Equipment* 602.1 (2009). Proceedings of the 3rd International Workshop on a Very Large Volume Neutrino Telescope for the Mediterranean Sea, pp. 76 –79. ISSN: 0168-9002. DOI: https://doi.org/10.1016/j.nima.2008.12.183. URL: http://www.sciencedirect.com/science/article/pii/S0168900208018299.

[36] G. D. Barr et al. "Uncertainties in atmospheric neutrino fluxes". In: *Phys. Rev. D* 74 (9 2006), p. 094009. DOI: 10.1103/PhysRevD.74.094009. URL: https://link.aps.org/doi/10.1103/PhysRevD.74.094009.

[37] P. Migliozzi and F. Terranova. "Learning from τ appearance". In: *New Journal of Physics* 13.8 (2011), p. 083016. DOI: 10.1088/1367-2630/13/8/083016. URL: https://doi.org/10.1088%2F1367-2630%2F13%2F8%2F083016.

[38] J. P. Yanez and A. Kouchner. "Measurement of Atmospheric Neutrino Oscillations with Very Large Volume Neutrino Telescopes". In: *Advances in High Energy Physics* 2015 (2015), p. 24. DOI: https://doi.org/10.1155/2015/271968.

[39] IceCube. 2019. URL: https://masterclass.icecube.wisc.edu/en/icetop/measuring-cosmic-rays.

[40] I. Esteban et al. "Updated fit to three neutrino mixing: exploring the accelerator-reactor complementarity". In: *Journal of High Energy Physics* 2017.1 (2017), p. 87. ISSN: 1029-8479. DOI: 10.1007/JHEP01(2017)087. URL: https://doi.org/10.1007/JHEP01(2017)087.

[41] C. Spiering. "Towards high-energy neutrino astronomy". In: *The European Physical Journal H* 37.3 (2012), pp. 515–565. ISSN: 2102-6467. DOI: 10.1140/epjh/e2012-30014-2. URL: https://doi.org/10.1140/epjh/e2012-30014-2.

[42] K. Kodama et al. "Observation of tau neutrino interactions". In: *Physics Letters B* 504.3 (2001), pp. 218 –224. ISSN: 0370-2693. DOI: https://doi.org/10.1016/S0370-2693(01)00307-0. URL: http://www.sciencedirect.com/science/article/pii/S0370269301003070.

[43] P. Lamare. private communication. CCPM.

[44] S. Hallmann. priveta communication. Friedrich-Alexander-Universität Erlangen, ECAP.

[45] L. Breiman. "Random Forests". In: *Machine Learning* 45.1 (2001), pp. 5–32. ISSN: 1573-0565. DOI: 10.1023/A:1010933404324. URL: https://doi.org/10.1023/A:1010933404324.

A Appendix

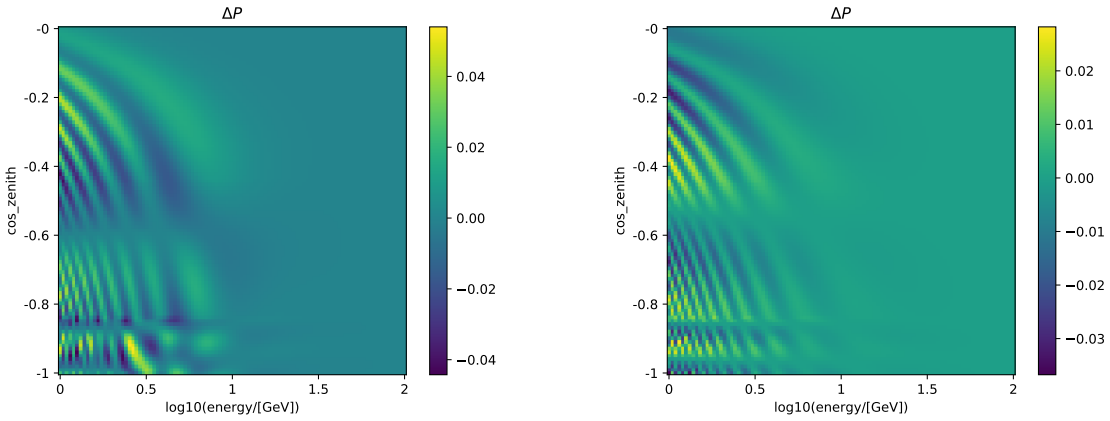

(a) $\Delta P(\nu_{mu} \to \nu_\tau)$ (b) $\Delta P(\bar{\nu}_{mu} \to \bar{\nu}_\tau)$

Figure A.1: Differences in the oscillation pattern with $\delta_{\mathrm{CP}} = 0°$ and $\delta_{\mathrm{CP}} = 305°$. The energy-zenith region relevant for ν_τ-appearance studies are not affected (see section 3.5).

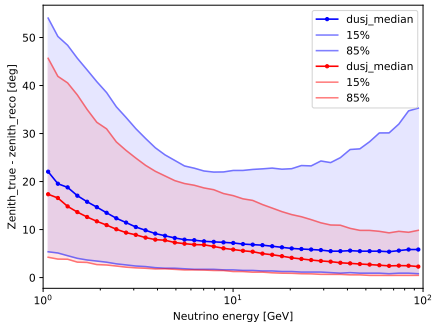

(a) Zenith resolution.

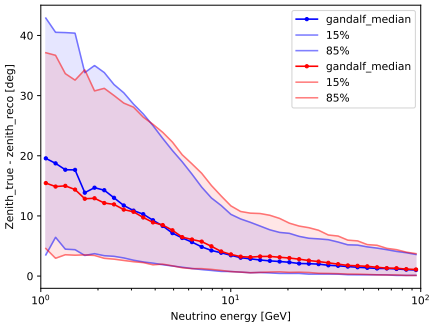

(a) Zenith resolution.

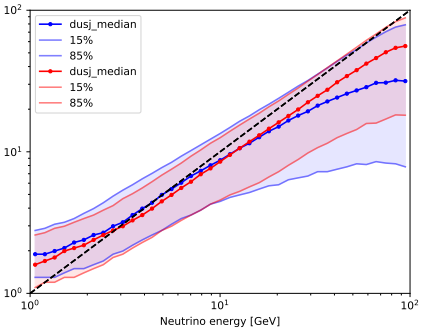

(b) Energy resolution.

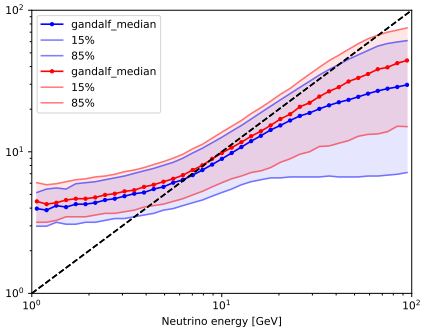

(b) Energy resolution.

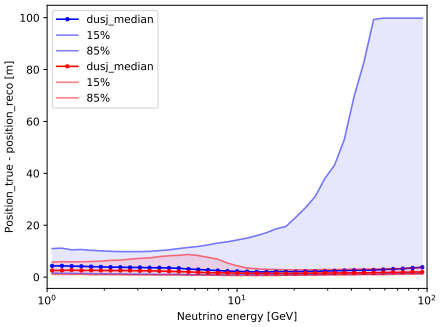

(c) Position resolution.

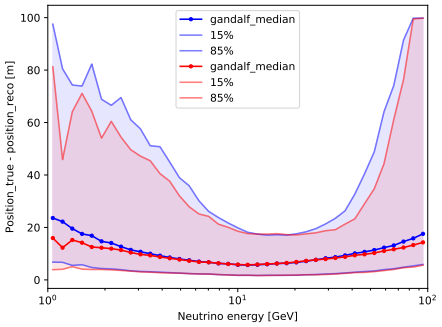

(c) Position resolution.

Figure A.2: 115DU: Resolution plots comparing selected (red) with deselected (blue) shower-like-events.

Figure A.3: 115DU: Resolution plots comparing selected (red) with deselected (blue) track-like events.

Selection criteria are among others energy, position and fit likelihood of the reconstruction algorithm.

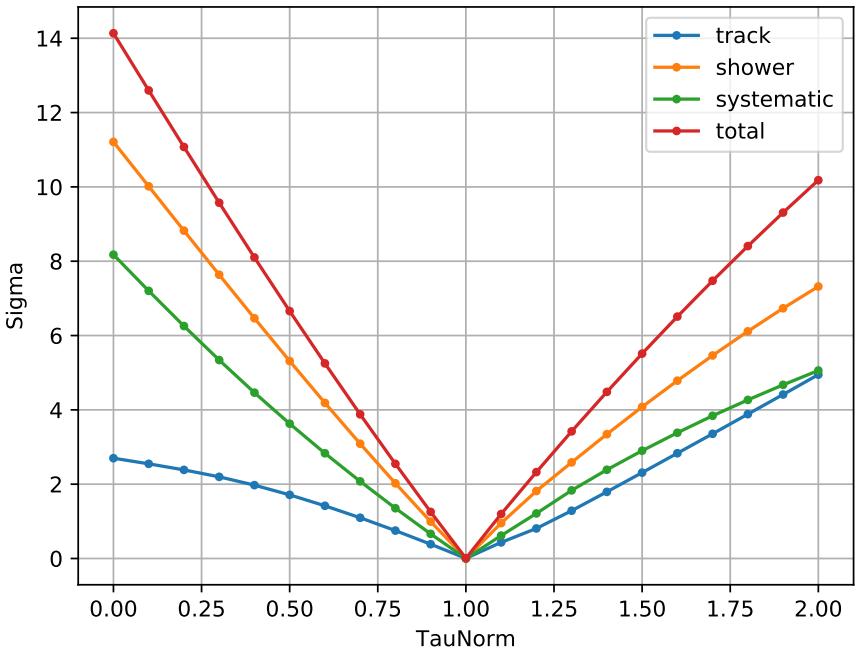

Figure A.4: Composition of the final TauNorm profile from the track channel, shower channel and systematic error. Since most ν_τ are reconstructed as shower-like, the biggest contribution comes from the shower channel.

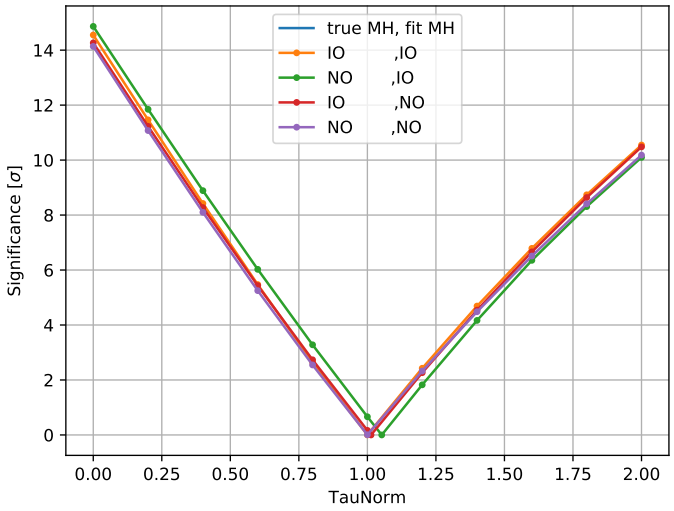

Figure A.5: Correlation between mass hierarchy and ν_τ-sensitivity. For the four presented SWIM runs different combinations of true and expected mass hierarchies were tested. IO=inverse ordering, NO=normal ordering. The resulting error is $< 5\%$.

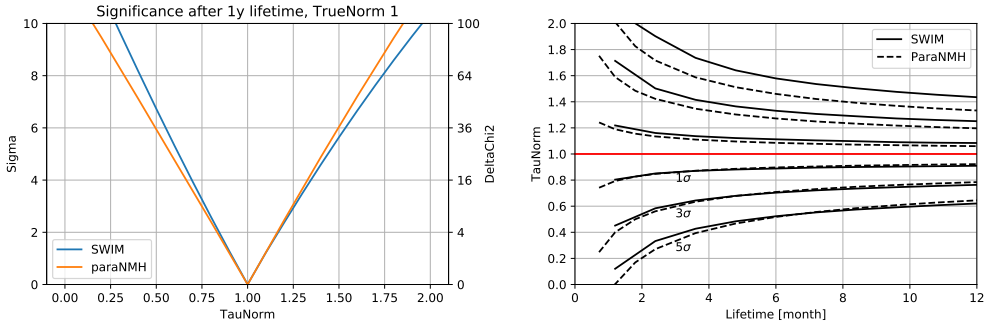

(a) TauNorm exclusion after one year detector lifetime.

(b) TauNorm exclusion over liftetime of detector. Black lines mark the $1\,\sigma$, $3\,\sigma$ and $5\,\sigma$ exclusion significance.

Figure A.6: ν_τ-sensitivity results of SWIM and ParaNMH for the full ORCA detector after one year live-time. For the simulated data true TauNorm = 1 and normal hierarchy were assumed. The differences come from different treatment of flux normalisations.

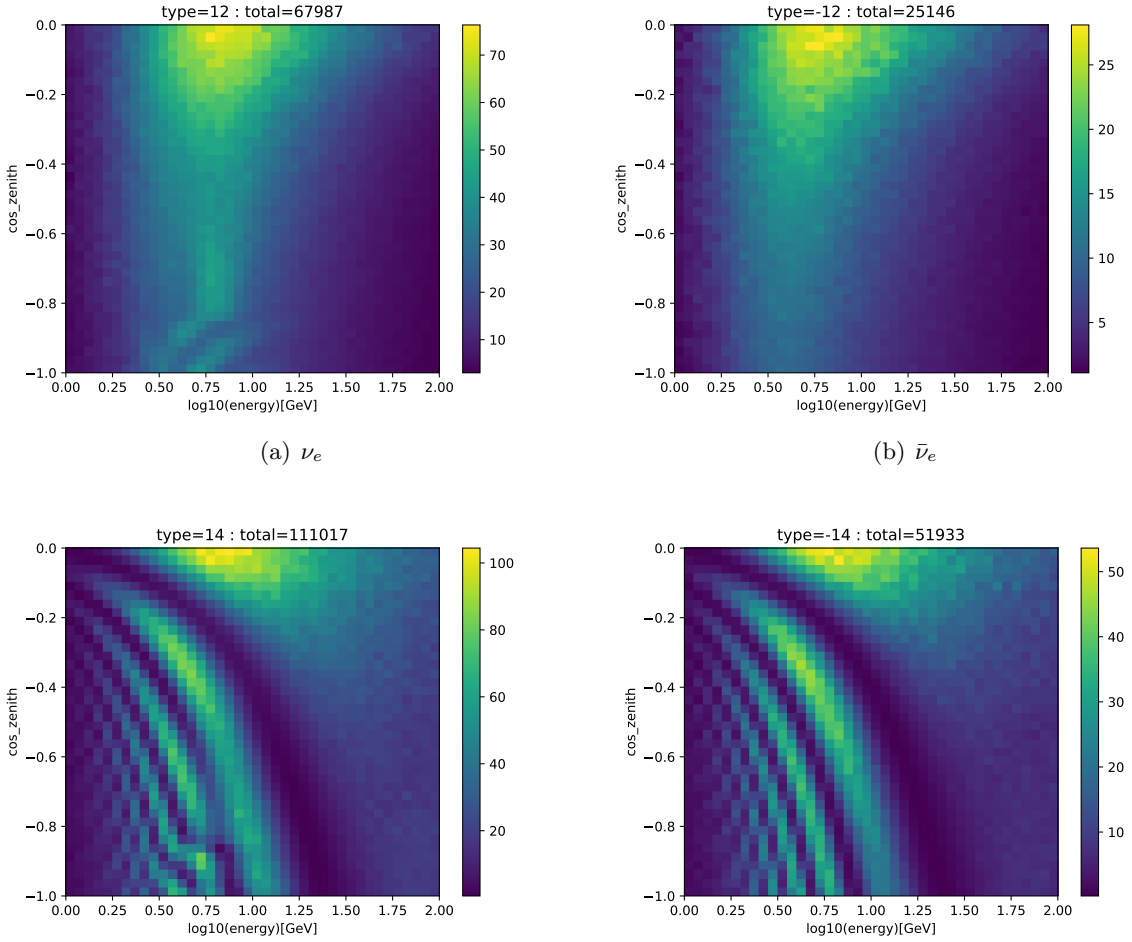

(a) ν_e (b) $\bar{\nu}_e$

(c) ν_μ (d) $\bar{\nu}_\mu$

Figure A.7: Expected event rates in ORCA 115DU for one year.

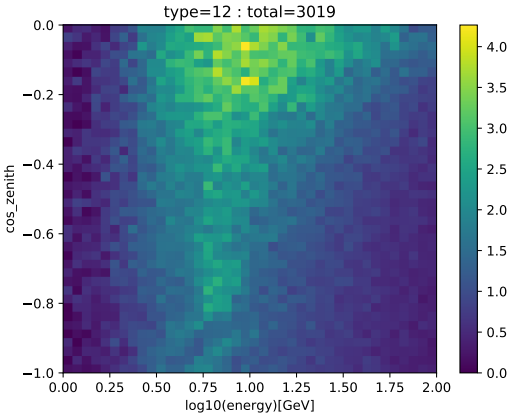

(a) ν_e

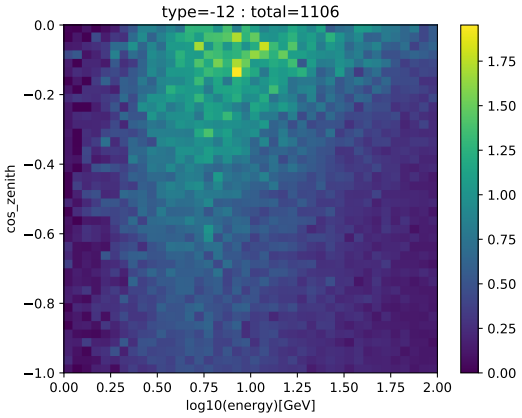

(b) $\bar{\nu}_e$

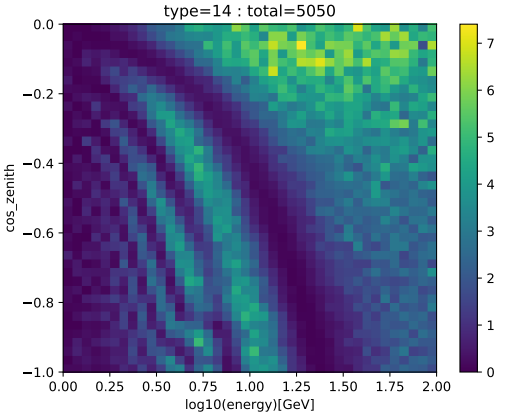

(c) ν_μ

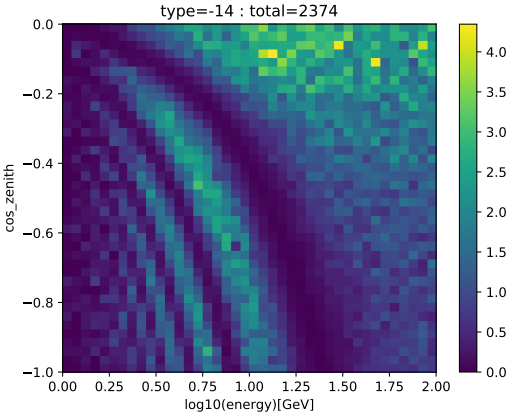

(d) $\bar{\nu}_\mu$

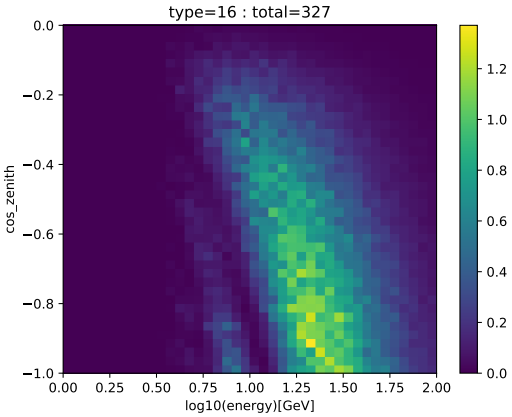

(e) ν_τ

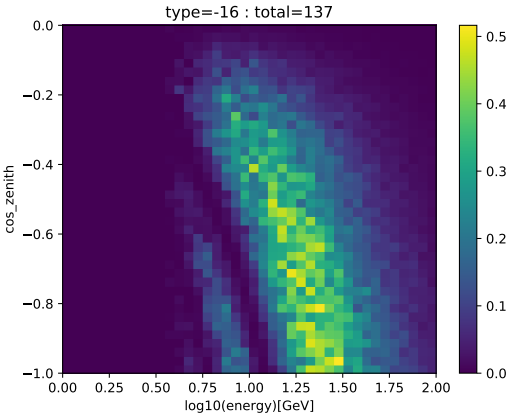

(f) $\bar{\nu}_\tau$

Figure A.8: Expected event rates in ORCA 7DU for one year.

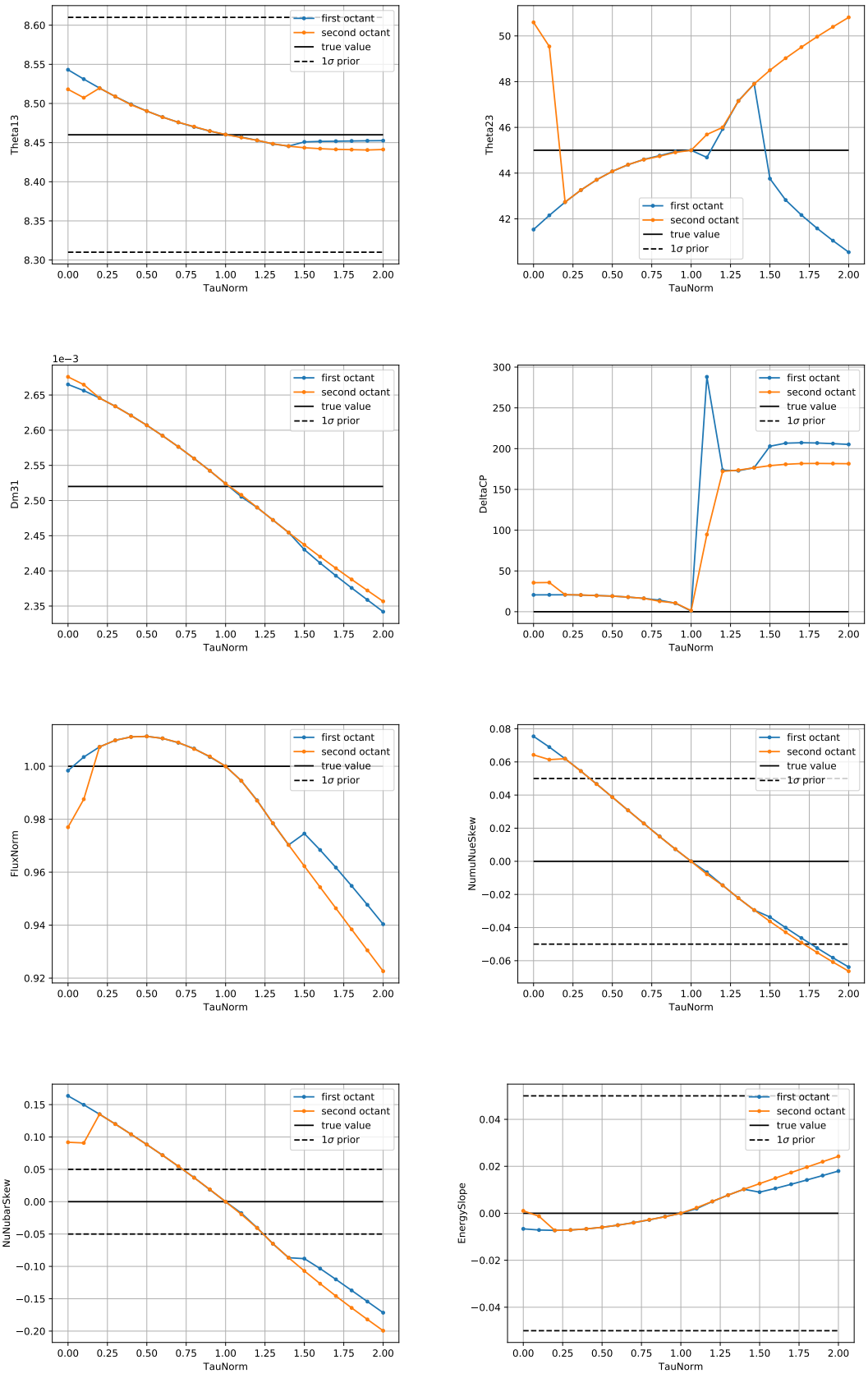

Figure A.9: See Figure 4.8.

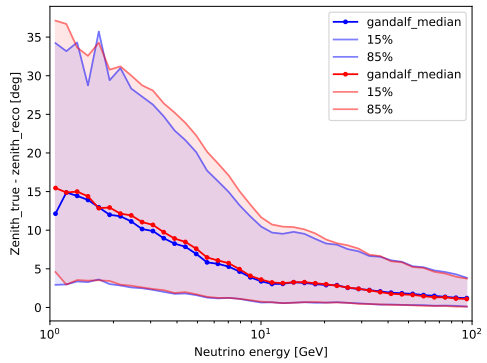

(a) Zenith resolution

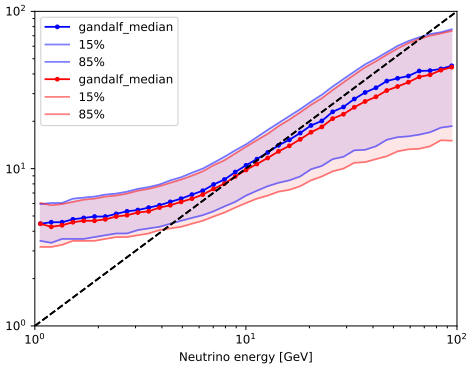

(b) Energy resolution

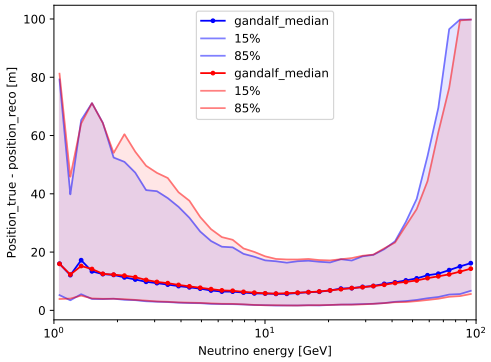

(c) Position resolution

Figure A.10: Resolution of track-like events, whose endpoint is reconstructed inside a can with dimensions $r = 150\,\mathrm{m}$ and $h = 100\,\mathrm{m}$ inside the instrumented volume.

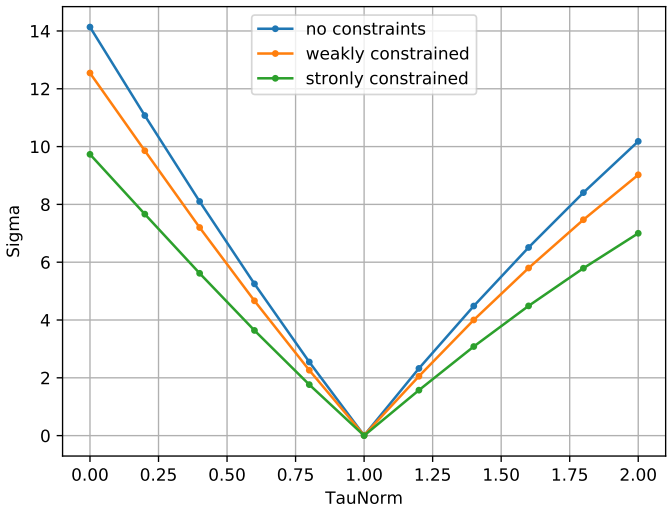

Figure A.11: TauNorm profile for two constraints on the endpoint position for track-like events. Although these events have better resolutions (fig. A.10), the ν_τ-sensitivity gets worse, due to the lower statistic (60% - 40% of original data).

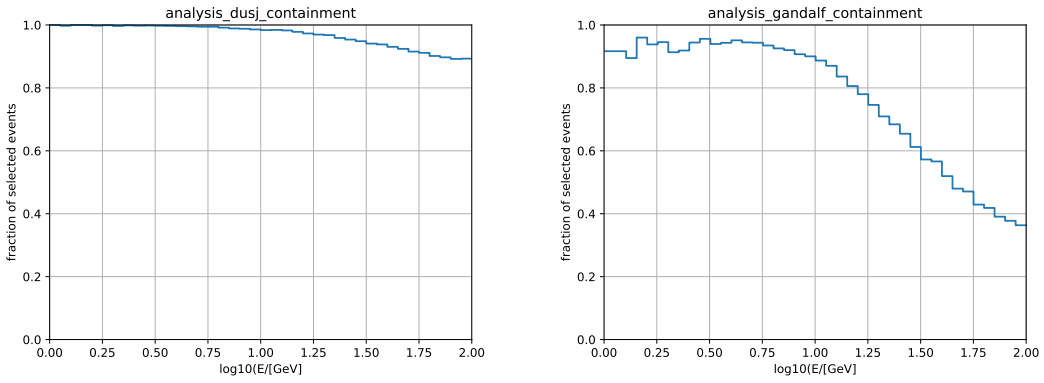

(a) Shower-like (b) Track-like

Figure A.12: Containment: Fraction of selected simulated events over energy.

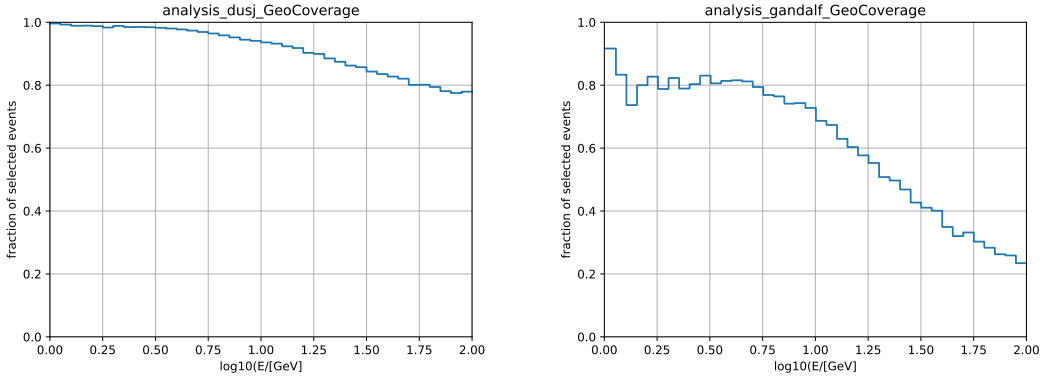

(a) Shower-like (b) Track-like

Figure A.13: GeoCoverage: Fraction of selected simulated events over energy.

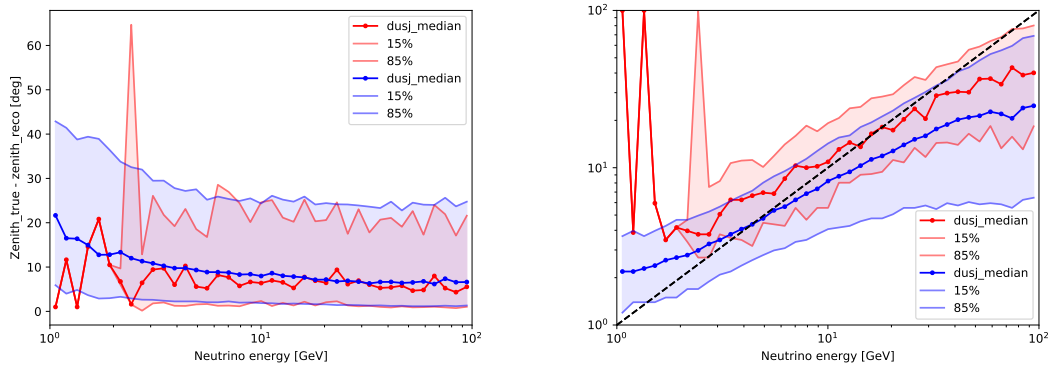

(a) Zenith resolution (b) Energy resolution

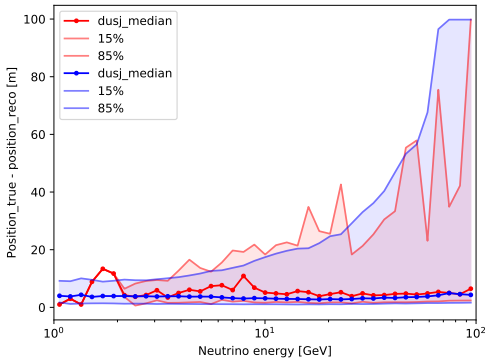

(c) Position resolution

Figure A.14: Containment: Resolution of contained (blue) vs. deselected (red) shower-like neutrino events. Note that the deselected statistics for energies $< 3\,\mathrm{GeV}$ are insufficient.

Danksagung

Hiermit möchte ich mich bei allen Menschen bedanken, die mich während meiner Arbeit unterstützt haben. Allen voran meinem Betreuer PD Dr. Thomas Eberl, der mir die Mitwirkung an einem so faszinierendem Projekt ermöglicht hat. Außerdem danke ich Jannik Hofestädt für seine Unterstützung, vor allem während der Schlussphase der Arbeit. Ganz besonderer Dank geht an Steffen Hallmann, der mir von Anfang an zur Seite stand, mich in meine Arbeit eingeführt hat und stets zu allen Fragen eine Antwort hatte. Danke an die gesamte Neutrinogruppe des ECAP, danke an Jutta Schnabel für die Gesellschaft die letzten Wochen und die Versorgung mit Keksen. Danke an Prof. Dr. Gisela Anton für die Übernahme der Zweitkorrektur. Zu guter letzt danke ich natürlich meinen Eltern, die sich zwar nicht für Neutrinos interessieren, mir aber trotzdem die letzten Jahre mein Physikstudium ermöglicht haben.

Erklärung

Hiermit versichere ich, dass ich die vorliegende Arbeit selbstständig verfasst und keine anderen als die angegebenen Quellen und Hilfsmittel benutzt habe, dass alle Stellen der Arbeit, die wörtlich oder sinngemäß aus anderen Quellen übernommen wurden, als solche kenntlich gemacht sind und dass die Arbeit in gleicher oder ähnlicher Form noch keiner Prüfungsbehörde vorgelegt wurde.

Erlangen, den 16.5.2019